

REMOTE SENSING REVIEWS

Forthcoming issues

Remote Sensing of the Ocean Surface

Interaction of Electromagnetic Waves with Canopy

Interpretation of Thermal Infrared Data: the Heat Capacity Mapping Mission

KSRVEP 1(1) 1-186 (1983)
ISSN: 0275-7257
ISBN: 37186-0132-X
Volume 1, Part 1 (1983)

REMOTE SENSING REVIEW

Editor-in-Chief: FRANÇOIS BECKER

Issue

1 Radar Remote Sensing

Page 1	Editorial <i>F. Becker</i>
3	Introduction and Some General Aspects of Image Formation in Radar Remote Sensing <i>G. P. de Loor</i>
19	Side-looking Radar, a Tool for Geological Surveys <i>B. N. Koopmans</i>
71	Photogrammetric Aspects of Remote Sensing with Imaging Radar <i>F. W. Leberl</i>
159	Introduction to the Use of Radar in Remote Sensing <i>L. Krul</i>
179	Some Remarks on the Status of Radar Remote Sensing <i>G. P. de Loor</i>
181	Subject Index

Issue Editor: G. P. de LOOR

SECTION 3

Photogrammetric Aspects of Remote Sensing with Imaging Radar

FRANZ W. LEBERL

Technical University and Graz Research Center, A-8010 Graz, Austria

1 INTRODUCTION

Side-looking radar (SLR) has become the essential imaging device to be used for radar remote sensing. Circularly scanning radar (plan-position indicator, PPI) has been studied to some extent in the 1950s and 60s (Rinner, 1948; Protherse *et al.*, 1950; Macchia, 1957) but today has no role in remote sensing. SLR has in the past been used extensively for rapid reconnaissance-type mapping of vast, previously unexplored regions of the continents, and for the study of ocean phenomena. As a result, SLR image maps at scale of about 1:250,000 were generated for entire countries such as, for example, Brazil (de Azevedo, 1971), Venezuela (McKeon, 1979), Panama (Crandall, 1968), Guatemala, Nigeria and Togo (Dellwig, 1980), and for portions of other countries such as Indonesia (Froidevaux, 1980), the Philippines, Colombia (Leberl, 1974), Peru (Martin-Kaye, 1980), the U.S.A. and others. SLR clearly was the most "operational" new remote sensing device (apart from photography) until the advent of Landsat remote sensing (Mathews, 1975).

In spite of this fact research workers in the geo-science area did not stress investigations with SLR-data. The emphasis was instead on remote sensing with passive sensors, in particular on aircraft multispectral scanning (MSS), and since 1972 on Landsat-MSS. This has somewhat changed towards the end of the last decade. The question of the usefulness of SLR for geoscience applications is being investigated by an increasing number of scientists. The trend can be observed in the U.S., with NASA and other agencies (Radar Geology, 1980), in Europe with

ESA and its co-operative research projects, and in Japan. Anticipated applications of this work are not only seen in exploratory mapping, but in the detailed study and monitoring of changing phenomena, such as vegetation, inundation, sea-ice and others. A noticeable slant towards radar studies was evident in a recent IEEE-conference on "new frontiers in remote sensing" (1981).

The reason for this interest may well be the independence from weather: after all, even Landsat-type imaging with an interval of 9 days between repeat coverages of a given area did not, in many areas of the world, provide sufficient useful images for monitoring-tasks and multi-temporal studies. Of a given area in Austria, to give just one example, there is no cloud-free Landsat image at all during the year 1980.

The increased thoroughness of SLR research has led to a need for better geometry, so that radar images can be compared to other data and to images taken at different times. While early radar maps were compiled with little attention to geometric accuracy, there is now an interest emerging in techniques of radar photogrammetry, or "radargrammetry", a term coined by Levine (1960), then still in the context of the plan position indicator.

A considerable motivation for active microwave imaging research for geoscience applications derives from satellite radar imaging. The first such projects were the Apollo Lunar Sounder Experiment in the Apollo Mission (Phillipps *et al.*, 1973), and then the SEASAT satellite in 1978 (Teleki *et al.*, 1978). Another project was the first launch of the space-Shuttle with a pay-load (Shuttle Imaging Radar, SIR-A). Planned missions are in Spacelab, in freeflyers such as the European Earth Resources Satellite ERS-1 (ESA, 1981), the Japanese Earth Resources Satellite ERS-1 (Ito, 1981) and the Canadian Sursat (Raney, 1981). Finally there is the exploration of the cloud-covered planet Venus in the Venus Orbital Imaging Radar (VOIR) and Venus Radar Mapper Projects (Leberl, 1981).

The radargrammetry aspects of SLR have even greater importance in these satellite projects than in imaging from aircraft because small neglects of these aspects already have great consequences on geometric accuracy. To give but one example, a satellite's velocity is roughly 40 times higher than an aircraft's; consequently a neglect regarding a function of time that is reasonable with aircraft radar may not be so when it is 40 times magnified in a satellite.

The current paper aims to present a review of geometric properties of

SLR images and of radargrammetry methods and results developed up to now. The topic is structured according to the basic radargrammetric units of the single image, stereo model and image block. Each point is complemented by the descriptions of results achieved in the past, and with considerations regarding satellite radar and results obtained from SEASAT-SLR images in mapping land and sea-ice.

The best geometric mapping accuracies obtained are of the order of magnitude of the geometric ground resolution. However, such accuracies were only obtainable in a controlled laboratory environment using considerable non-radar external data. In a more operational context, SLR has shown to provide geometric accuracies of about ± 100 m to ± 200 m in all three dimensions. To carry laboratory results into everyday practice would require improved sensor platform stabilisation and improvements of radar sensor design to satisfy photogrammetry requirements.

Lately, rather complex radargrammetric efforts were undertaken to simulate SLR-images from digital height models (Holtzman *et al.*, 1980; Naraghi *et al.*, 1981), and to cross-correlate simulated and actual SLR images for the purpose of precise pointwise rectification.

These lines of research indicate that requirements placed on SLR-image geometry are increasing. This is caused by the desire to utilize more fully the unique measurements taken by an SLR sensor. We may thus observe a development where geometric concepts are more important in the analysis of SLR-data than they are in other forms of remote sensing.

2 RELATING OBJECT AND IMAGE POINT COORDINATES

Radargrammetry requires a mathematical model relating an object point in some three-dimensional cartesian X, Y, Z coordinate system to the time and range coordinates, t and r , measurable from the side-looking radar record. Such models were presented and discussed by numerous authors, among them Konecny and Derenyi (1966), Akowitzki (1968), Derenyi (1970), Rosenfield (1968), Gracie *et al.* (1970), Leberl (1970), Hockeborn (1971), and Norvelle (1972). In all cases radargrammetry begins with the SLR-image, not with the raw electronic signals acquired by the antenna.

However, a trend in digital radar systems is developing to go beyond the radar record and to look into raw, unprocessed signals. First indications are visible in studies by Kratky (1979), Brown *et al.* (1981), and Curlander *et al.* (1981). These new approaches rely on concepts such as "sensor events time", i.e. the exact time when a raw pulse was transmitted from and received by the radar antenna, and how the raw radar echo is converted into image points.

2.1 Defining sensor events time t and slant range r for each image point

Figure 1 illustrates the concept of measurements taken on an SLR-recording or image: we measure for each image point P its x_k, y_k comparator coordinates or, if we deal with a digital image, its corresponding line and sample numbers. These need to be converted to the time, t , when object P was imaged (sensor events time), and range, r , to P . Numerous methods exist to relate x_k, y_k to r, t . Generally we may therefore just define an operator F :

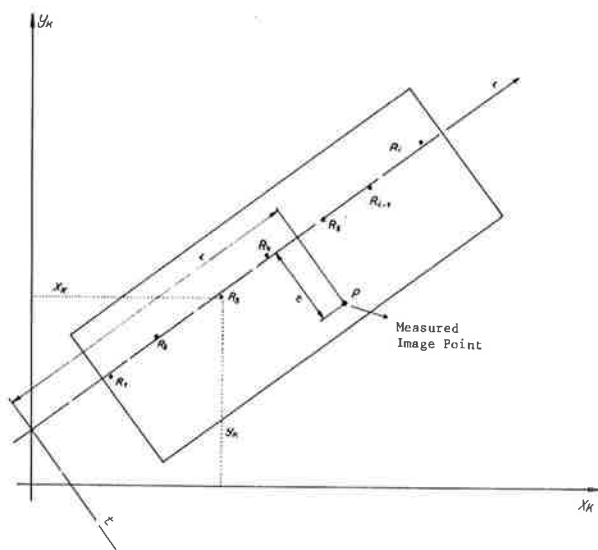


FIGURE 1 Measuring coordinates in a side-looking radar image; x_k, y_k are comparator coordinates, r, t are range and time coordinates.

$$r = F_r(x_k, y_k) \quad (1)$$

$$t = F_t(x_k, y_k)$$

In certain types of radar images, particularly those designed for good geometry, one may find auxiliary reference marks, such as those of Figure 1, denoted by R_1, R_2 etc. Depending on the type of marks we can define the form of Equ. (1) and its parameters. As an example, a single row of so-called time-marks may enable one to define a straight line to be denoted as "image time coordinate" axis, x . Perpendicular to it we may then select the image range coordinate axis, y :

$$y = (a_1 x_k - y_k + a_0) / (a_1^2 + a_0^2) \quad (2)$$

$$x = (x_k^2 + y_k^2 + a_0^2 - 2a_0 y_k^2 - y_k^2)^{1/2}$$

where a_0 and a_1 are the coefficients of a straight line. Knowing the time, t_i , associated with particular time marks, we find for a point P :

$$t_p = t_i + (t_{i+1} - t_i) \cdot (x_p - x_i) / (x_{i+1} - x_i) \quad (3)$$

With the known slant range, r_c , to the time marks, and to the straight line of Eq. (2), we find for point P :

$$r_p = (y_p + r_c) \cdot f \quad (4)$$

where f is a scale factor.

We do assume a so-called *slant-range presentation*, thus image distances between two points in range direction correspond to the difference of their distances from the antenna.

In the event of a *ground range presentation*, we denote the range-coordinate by y_g and find:

$$r_p = ((y_g / f^2 + e)^2 + H^2)^{1/2} \quad (5)$$

where H is the (nominal) flying height for conversion of slant to ground (or horizontal) distances, and e is the ground range equivalent to r_c .

The numerous different ways of defining and describing relationship (1) depend on the way the radar record is related to time and range. In the

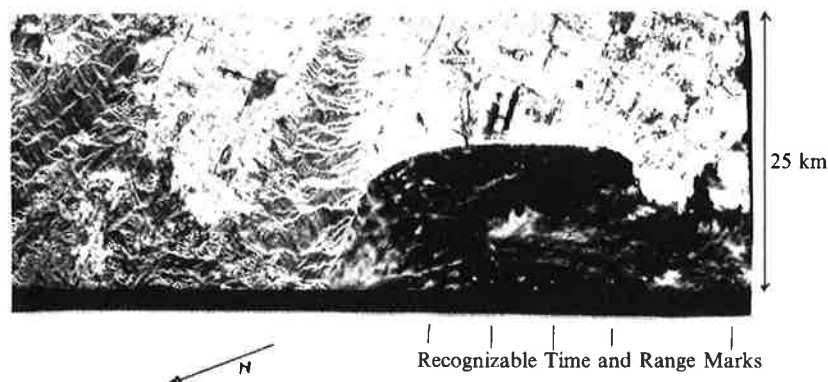


FIGURE 2 Example of an optically generated SEASAT-SAR image with time and range marks, showing Los Angeles, California.

optically generated SEASAT-Synthetic Aperture Radar (SAR) images, there were time and range marks to both sides of the image, according to Figure 2, so that the time and range to a point P could be found by linear interpolation with the surrounding 4 marks. A similar technique was used in the RAMP-imaging effort of Panama (Hockeborn, 1971).

For a long time the digitally correlated SEASAT-SAR images did not show any time or range reference marks. The user was not provided with means to enable him to relate x, y to t, r coordinates. However, Curlander (1981) recently established a relationship that exists between, on one hand, the sensor events time, t , and slant range, r , and, on the other hand, the image pixel line (azimuth) number i and sample (range) number j . This relationship is for digitally correlated SEASAT-SAR rather complex. This is illustrated by the formulas that were presented by Curlander (1981) who went back to the raw signal data to define r, t for each pixel. For each i, j image pixel he has to work with auxiliary pixel numbers i_s, j_s in the signal history record. Curlander's formulas are presented just to illustrate the complexity of the relationship. For full details reference has to be made to the author's original description of the system:

$$t = \frac{2048 + 4 \cdot i_s}{\text{PRF}} + t_0 \quad (6)$$

$$r = \frac{c}{2} (9 \cdot P + (N1 + 4 \cdot P)/64 - \text{const})$$

$$+ \frac{c}{f_1} \left(\frac{N2}{2} + j_s + 5 \cdot IS + \frac{IS}{256} (i_s - 1024 \cdot \text{INT}(i/1024)) \right) + \frac{\lambda}{4 f_D'} (f_{DD} - f_D)^2 \quad (7)$$

Pixel line and sample numbers, i_s, j_s , relate to a data block in the signal history data. We find in Eqs. (6) and (7) the pulse repetition frequency, PRF, and its inverse, P , the inter-pulse period. We have c , the velocity of electromagnetic energy; $N1$, a parameter of the sensitivity time control; half the sampling frequency f_1 ; processing parameters, $N2$ and IS ; the wavelength λ ; the Doppler frequency, f_D' ; the range walk or signal curvature correction, f_{DD} ; and the rate of Doppler frequency, f_D .

It is obvious from these equations that the inner geometry of a radar recording is comparatively complex. Clearly, though, one can also here simplify Eq. (7) to a form of Eq. (4), where the coefficients must be provided by the radar engineer.

2.2 Projection equation

Numerous authors have formulated rigorous radar projection equations, similar to the so-called rigorous photogrammetric equations for photography. The intent of these formulations is to model the typical range projection. Object points are projected along concentric circles onto a projection plane (Figure 3). Authors who have contributed here are Rinner (1948), Konecny and Derenyi (1966), Rosenfield (1968), Akowetzki (1968), Derenyi (1970), Gracie *et al.* (1970), Leberl (1970),

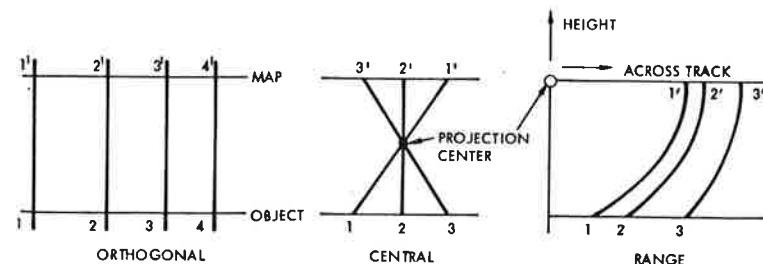


FIGURE 3 Range projection. Each image point defines a circle as the locus of the corresponding object point.

Hockeborn (1971), Norvelle (1971), Geier (1972), Greve and Cooney (1974), DBA-Systems (1974) and many authors since. A review was compiled by Leberl (1976b).

For such a formulation we need to define the sensor position, $\underline{s}(t) = (s_x(t), s_y(t), s_z(t))^+$, and antenna attitude with $\phi(t)$, $\omega(t)$, $\kappa(t)$. In synthetic aperture radar, the synthetic antenna's attitude is merely the first derivative of position, namely the velocity vector $\dot{\underline{s}}(t) = (\dot{s}_x(t), \dot{s}_y(t), \dot{s}_z(t))$. Both $\underline{s}(t)$ and $\dot{\underline{s}}(t)$ are functions of time t . The formulation also requires a definition of object- and sensor coordinate systems according to Figure 4, with unit vectors $\underline{e}_1, \underline{e}_2, \underline{e}_3$ and $\underline{u}, \underline{v}, \underline{w}$, respectively.

We then find for an object point P its position vector \underline{p} :

$$\underline{p} = p_x \underline{e}_1 + p_y \underline{e}_2 + p_z \underline{e}_3 \quad (8)$$

and in the sensor system

$$\underline{r} = u_p \underline{u} + v_p \underline{v} + w_p \underline{w} \quad (9)$$

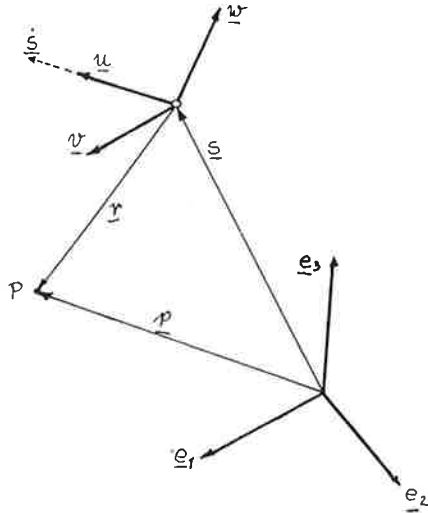


FIGURE 4 Definition of object space and sensor coordinate systems.

Therefore,

$$\underline{p} = \underline{s} + \underline{r} \quad (10)$$

It is straightforward to see from Figure 5 that

$$\begin{aligned} u_p &= r \sin \tau \\ v_p &= r(\sin^2 \Omega - \sin^2 \tau)^{1/2} \\ w_p &= -r \cos \Omega \end{aligned} \quad (11)$$

Auxiliary angle τ is a system constant called *squint-angle* by most authors (Rosenfield, 1968; Hockeborn, 1971) and defines the conical shape of the radar pulse.

Introducing a new vector $\underline{\bar{p}} = (u_p, v_p, w_p)$ in the sensor coordinate system and a rotation matrix $\underline{\bar{A}}$ to rotate the sensor system $\underline{u}, \underline{v}, \underline{w}$ into the object system $\underline{e}_1, \underline{e}_2, \underline{e}_3$, we find in matrix notation:

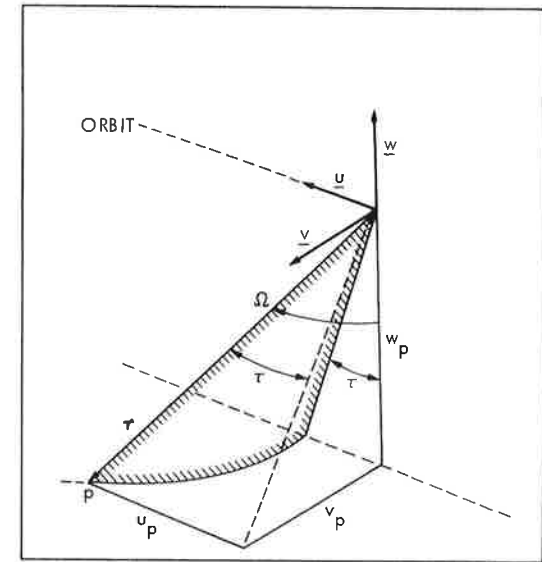


FIGURE 5 Relating squint angle τ , slant range r and elevation angle Ω to sensor coordinates u, v, w .

$$\underline{p} = \underline{s} + \underline{A} \cdot \underline{\bar{p}} \quad (12)$$

where

$$\underline{A} = \begin{bmatrix} u_x(t) & u_y(t) & u_z(t) \\ v_x(t) & v_y(t) & v_z(t) \\ w_x(t) & w_y(t) & w_z(t) \end{bmatrix} \quad (13)$$

Rotation matrix \underline{A} can contain the classical orientation angles ϕ , ω and κ if we deal with a real antenna. With synthetic antennas, we obtain:

$$\begin{aligned} \underline{u} &= (u_x, u_y, u_z) = \underline{\dot{s}}/|\underline{\dot{s}}| \\ \underline{v} &= (v_x, v_y, v_z) = (\underline{s} \times \underline{\dot{s}})/|\underline{s} \times \underline{\dot{s}}| \\ \underline{w} &= (w_x, w_y, w_z) = (\underline{u} \times \underline{v})/|\underline{u} \times \underline{v}| \end{aligned} \quad (14)$$

The unit vector \underline{u} extends along the synthetic antenna, thus in the direction of the velocity vector $\underline{\dot{s}}$. The unit vector \underline{v} should be normal to \underline{u} and to the nadir direction of the antenna. For satellite sensors, the nadir direction is easily seen to be the direction of the sensor position vector in a planetocentric system. With aircraft radar, one has to specify here explicitly that a geocentric system is assumed also for the sensor position vector \underline{s} and the object coordinate system defined by $\underline{e}_1, \underline{e}_2, \underline{e}_3$.

Equations (11) and (12) relate object and image, where r and time t derive from the image coordinates. We now see that—contrary to classical photogrammetry—we do not algebraically relate image and object coordinates, but the image only defines time, which in turn defines the parameters \underline{s} and \underline{A} of Eq. (12).

If the imaging arrangement, and thus $\underline{s}(t)$, $\underline{A}(t)$, are known (measurement of navigation data), then we have for each point 3 equations (Eq. 12) with 4 unknowns i.e. Ω , p_x , p_y and p_z . It may be preferable to work with 2 equations and 3 unknowns. This is achieved by elimination of the unknown elevation angle Ω (angle between nadir and line of sight), thus giving the following two equations:

$$|\underline{p} - \underline{s}| = r \quad (15)$$

$$\underline{u} \cdot (\underline{p} - \underline{s}) = \sin \tau |\underline{u}| |\underline{p} - \underline{s}| = \sin \tau \cdot r \quad (16)$$

where we now have a simple geometric description of the radar projection case. The geometric locus of a point is the intersection of *range-sphere* (Eq. 15) with a *cone* (Eq. 16). This is the circular projection line mentioned before.

In Eq. (16) the sensor coordinate axes are all described by the geometric position and velocity vector of the antenna. This applies in particular for SAR, since the antenna attitude is defined by the velocity vector, (the “synthetic” antenna extends in the direction of the physical antenna’s motion). For real aperture radar, the real antenna’s attitude itself is to be used to define \underline{u} , \underline{v} and \underline{k} . Therefore angles ϕ and κ must be entered in Eq. (13); ω is insignificant and can be set at zero. This is obvious from Eqs. (15) and (16) which do not contain an angle ω since the components of vector \underline{u} in the rotation matrix \underline{A} , namely u_x , u_y and u_z do not contain ω . The same fact is also obvious from geometry: the projection circle is not affected by a sensor roll, ω .

2.3 The squint angle τ

In aircraft radar, τ normally is zero, so the cone of Eq. (16) degenerates to a scanning plane:

$$\underline{u} \cdot (\underline{p} - \underline{s}) = 0 \quad (17)$$

The range sphere has an obvious physical explanation: the echo-time measurement of radar clearly associates with each image point a slant range r , and therefore a sphere, as one geometric locus for the corresponding object (Figure 6).

The cone is slightly more difficult to explain: with synthetic aperture radar, image generation requires an operator or algorithm to specify the precise Doppler-frequency with respect to which the echo signals should be converted to an image. Should this Doppler frequency be 0, then Eq. (17) applies. Should the Doppler frequency not be 0, then the radar is either looking ahead (> 0) or back (< 0). All points ahead of (or behind) the sensor which generate radar echoes of one given Doppler frequency are on a specific conical surface. The cone angle is $180^\circ - 2 \cdot \tau$, where τ is the squint angle. The situation is illustrated in Figure 7.

The conical shape can be expressed also by the equation for the

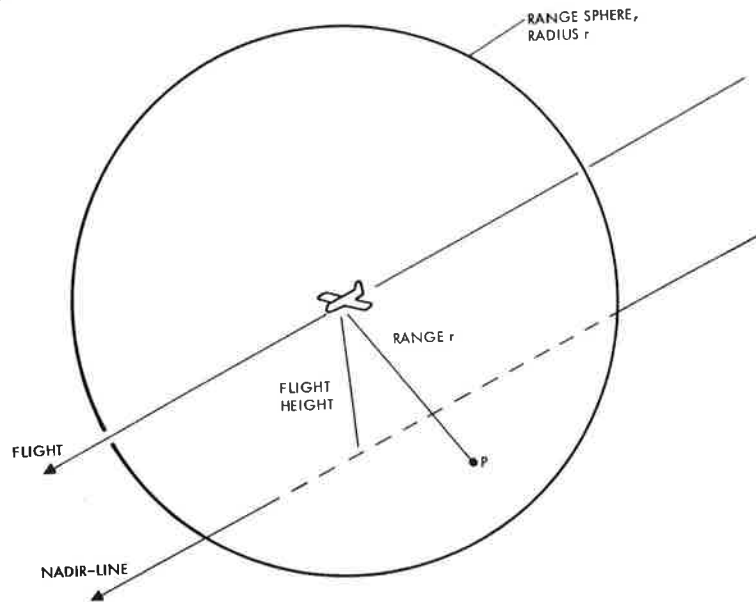


FIGURE 6 Range sphere.

Doppler frequency, f_D :

$$f_D = \frac{2}{\lambda \cdot r} \cdot u \cdot (s - p) \quad (18)$$

where λ is the wavelength and the squint angle results from:

$$\sin \tau = \frac{\lambda \cdot f_D}{2} \quad (19)$$

Equation (18) is equivalent to Eq. (16) replacing the geometric concept of the squint angle by the physical concept of Doppler-frequency.

One may ask the question why one may wish to generate radar images with a Doppler frequency $\neq 0$, or with a squint. The reason in the case of a satellite is simple: due to Earth rotation, the ground points with zero-Doppler frequency echoes are ahead or behind the plane perpendicular to the orbit plane and the satellite. The radar pulses, however, are sent in the direction of that plane. No radar signal may go into the direction of

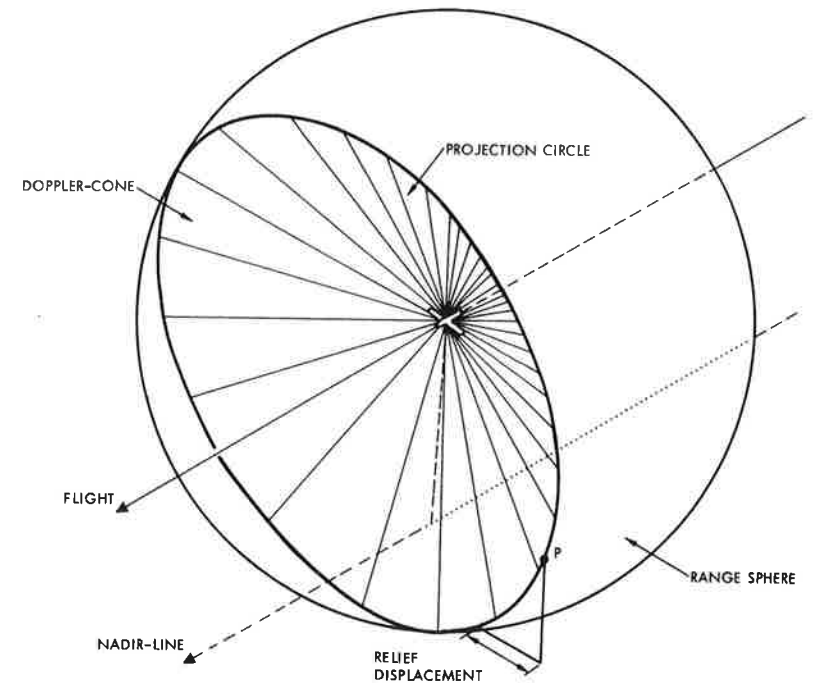


FIGURE 7 Range sphere and Doppler cone together define the projection circle.

zero Doppler (Figure 8). In order to get an image at all, the radar has to look ahead or back (perpendicular to the real antenna, not perpendicular to the velocity vector or the synthetic antenna). This is why satellite radar heavily depends a correlation with a squint τ , where τ is a function of time, $\tau(t)$. However, τ either is operator-selected or a controlled function of the planet's latitude and therefore well known.

2.4 Real aperture radar with squint and inclined imaging planes

Real aperture radar image generation is straightforward; geometric concepts are clear, since the image geometry is established during data acquisition and recording. A squinted imaging mode is feasible (Hockeborn, 1971), and so is imaging in an inclined plane, by merely tilting the antenna for an angle ϕ_0 around the \underline{v} -axis, or κ_0 around the \underline{k} -axis.

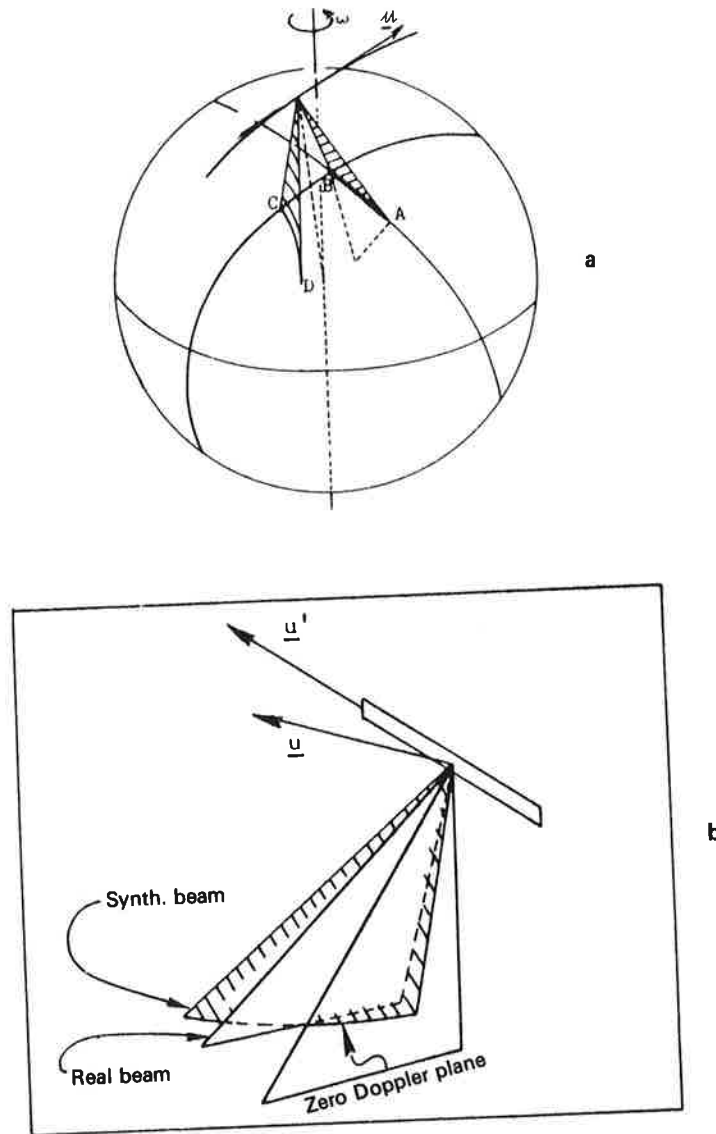


FIGURE 8 Satellite radar with zero-Doppler plane and the plane perpendicular to the orbit: (a) AB are in the plane perpendicular to the orbit plane, CD are perpendicular to the velocity vector with respect to the rotating earth; and (b) \underline{u}' is direction of the real antenna, \underline{u} is the velocity vector.

This is geometrically described by a rotation matrix \underline{R}_0 :

$$\underline{R}_0 = \begin{bmatrix} \cos \phi_0 \cos \kappa_0 & -\sin \kappa_0 & \sin \phi_0 \cos \kappa_0 \\ \cos \phi_0 \sin \kappa_0 & \cos \kappa_0 & \sin \phi_0 \sin \kappa_0 \\ -\sin \phi_0 & 0 & \cos \phi_0 \end{bmatrix} \quad (20)$$

These imaging modes are significant in forward-looking radars and were considered for specific stereo arrangements (see Bair and Carlsson, 1975).

2.5 The concept of inner orientation

The parameters of the relationship between image coordinates x, y and the object space entities r, t are denoted as *parameters of interior orientation*. Equations (2) to (7) all were mathematical representations of this interior orientation. The concept derives from photogrammetric cameras, where each image point defines a projection ray attached to the camera. The *exterior orientation* relates the projection ray to the object point.

However, Eqs. (2) to (7) represent merely a model of reality. Errors of this model must be anticipated as shown in Figure 9. Of course, any error model has unknown coefficients and the question is how to obtain estimates of these coefficients. As will be shown later, these can derive from known object point coordinates. Error models generally imply a polynomial form of the image coordinate deformation $\Delta r, \Delta t$. Gracie *et al.* (1970), Leberl (1971), DBA-Systems (1974) and others have applied the following polynomials:

$$\begin{aligned} \Delta r &= a_1 r + a_2 r^2 + a_3 r^3 + \dots \\ \Delta t &= b_0 + b_1 \cdot t + b_2 \cdot t^2 + b_3 \cdot t \end{aligned} \quad (21)$$

Little research exists on the various alternatives available to describe $\Delta r, \Delta t$ -errors in an optimum form. At this point one can therefore only direct attention to the fact that these errors must be somehow considered in radargrammetry.

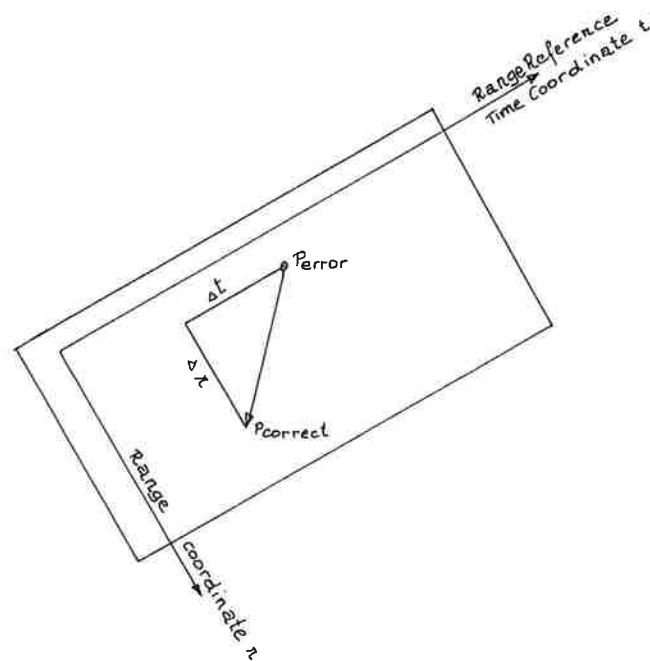


FIGURE 9 Radar interior orientation and image deformations Δr , Δt .

2.6 Discussion

The existing body of radargrammetric definitions for the projection equations relate to analog aircraft radar. Discussions concentrate on the use of time and range references. The situation is potentially different in satellite radar. So far, little has appeared on satellite radargrammetry although more work needs to be done due to the expected future significance of orbital imaging radars. Essential additions in this area are definitions of satellite radar imaging equations not merely as a function of sensor position and attitude, but as a function of orbital parameters such as orbit inclination i , radius a and eccentricity e of the orbit, the angle α of the line of apsides, time t and rotation velocity w of the Earth.

This may serve for image simulations and general radargrammetric analysis. Its discussion goes beyond the scope of this paper. Some work in this area has been done by Manning and Hann (1967) and by Leberl (1978a).

3 PLOTTING FROM SINGLE RADAR IMAGES

Work with SLR-images involves positioning efforts. This requires that details on the image are located in a geographic reference system. Single radar images are the basic unit of data for this work. Geographic "referencing" may result in the following:

- computation of ground coordinates from given image coordinates;
- generation of a grid overlay over a given image; and
- production of a rectified image, a so-called "ortho-image", using as an input a raw, distorted image and information on the object.

In the following we will discuss methods and results for these various single-image tasks.

3.1 Computation of ground coordinates from given image coordinates with known interior and exterior orientation

Equations (12) and (15, 16) described the relationship between object points \underline{p} and image or sensor entities. We have, with known orientation elements \underline{s} , \underline{A} and τ , or \underline{s} , τ and \underline{u} , a total of 3 equations with 4 unknowns, $\underline{p} = (p_x, p_y, p_z)$, and depression angle Ω in the formulation of Eq. (12), or of 2 equations with 3 unknowns, $\underline{p} = (p_x, p_y, p_z)$, in the formulation of Eqs. (15, 16).

We prefer the more compact version in Eqs. (15, 16). From a single two-dimensional image, we cannot reconstruct all 3 unknown coordinates p_x, p_y, p_z . A condition must be available for the object that relates p_x, p_y and p_z , or one coordinate must be known (e.g. p_z), so that the other two can be computed.

3.1.1 The object is an ellipsoid For a given image point, x_k, y_k coordinates are converted to r, t -values. With time t , the sensor position $\underline{s}(t)$ and velocity vector $\dot{\underline{s}}(t)$ or attitude $\phi(t), \kappa(t)$ can be generated. This then leads to 3 equations of the following form:

$$r = |\underline{p} - \underline{s}| = \sqrt{(p_x - s_x)^2 + (p_y - s_y)^2 + (p_z - s_z)^2} \quad (22)$$

$$\sin \tau = \underline{u} \cdot (\underline{p} - \underline{s}) / |\underline{p} - \underline{s}|$$

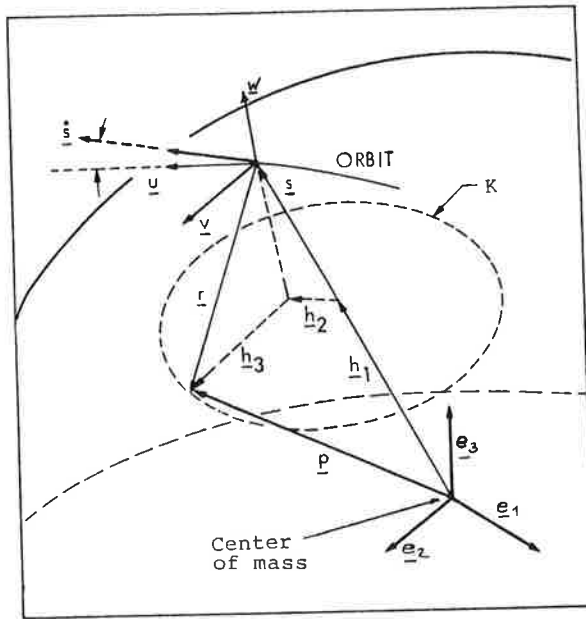


FIGURE 10 Intersecting a radar projection ray with a sphere.

$$= \{u_x(p_x - s_x) + u_y(p_y - s_y) + u_z(p_z - s_z)\} / r \quad (23)$$

$$(p_x^2 + p_y^2) / R_e^2 + p_z^2 / R_p^2 = 1 \quad (24)$$

where R_e and R_p are the planetary radius at the equator and pole, respectively. These are three non-linear equations with three unknowns, p_x , p_y and p_z . A solution can be obtained in an iterative procedure, starting from approximate values p_{x_0} , p_{y_0} and p_{z_0} .

3.1.2 The object is a sphere The above iterative solution can be avoided if the object is a sphere. This sphere can be a valid model even if the planetary surface is more precisely modelled by an ellipsoid. A sphere can be used to obtain good approximations for the iterative solution of Eqs. (22) to (24), or the ellipsoid is approximated by a sphere whose position and radius are optimized for a certain area. Figure 10 illustrates, that an object point p results from:

$$\underline{p} = \underline{h}_1 + \underline{h}_2 + \underline{h}_3 \quad (25)$$

$$h_1 = \underline{s} \cdot (R^2 + s^2 - r^2) / (2s^2) \quad (26)$$

where $|p|$ is the planetary radius, R , and s is the length of the position vector \underline{s} .

$$\underline{h}_2 = \{(s - h_1) \tan \alpha + l\} \cdot \underline{u} \quad (27)$$

where

$$\underline{u} = (\underline{s} \times \underline{v}) / |\underline{s} \times \underline{v}|$$

and

$$\underline{v} = \underline{s} \times \dot{\underline{s}} / |\underline{s} \times \dot{\underline{s}}|$$

$$\underline{h}_3 = \{(r^2 - h_2^2 - (s - h_1)^2)^{1/2}\} \cdot \underline{v} \quad (28)$$

Vector \underline{v} is a unit vector perpendicular to the orbit plane formed by the position vector \underline{s} and velocity vector $\dot{\underline{s}}$; \underline{u} is an auxiliary vector mutually perpendicular to \underline{s} and \underline{v} . Angle α is formed between \underline{u} and \underline{u} :

$$\cos \alpha = \underline{u} \cdot \underline{u}$$

Entity l is auxiliary to account for the effect of a squint angle τ . A somewhat involved procedure is required to compute l :

$$l = \sin^2 \bar{\tau} - m \pm (m^2 - (m^2 - b^2 - h_3^2) / \sin^2 \bar{\tau})$$

where

$$\cot \bar{\tau} = (\cot^2 \tau - \tan^2 \alpha) / \cos \alpha$$

$$m = (s - h_1) \cdot \tan \alpha$$

$$b = \cot \bar{\tau} \cdot a$$

$$a = \sin \tau \cdot (s - h_1) / \cos \alpha \cdot \cos(\tau + \alpha)$$

A derivation is beyond the scope of this paper; it has been presented in a report by Leberl (1978a). However, for $\tau = 0$ we find $l = 0$.

We have thus now a procedure available to directly compute vector $\underline{p} = (p_x, p_y, p_z)$ from image data r , t and orientation parameters τ , $\underline{s}(t)$ and $\dot{\underline{s}}(t)$.

3.1.3 *The object is a horizontal plane* In the event of an aircraft radar we may approximate the ground surface by a plane $p_z = 0$:

$$r^2 = (p_x - s_x)^2 + (p_y - s_y)^2 + s_z^2 \quad (29)$$

$$\sin \tau \cdot r = u_x(p_x - s_x) + u_y(p_y - s_y) - u_z s_z$$

This results in an equation of 2nd order with four solutions. It will be apparent from the general imaging configuration which solution should be taken.

3.1.4 *Horizontal flight and object plane* Equation (29) further simplifies if the antenna attitude is parallel to the $\underline{e}_1, \underline{e}_2$ -coordinate axes. In this case we find $u_x = \cos \kappa$, $u_y = \sin \kappa$ and $u_z = 0$. If we also assume a ground coordinate system with an x -axis parallel to the flight direction, we obtain:

$$\begin{aligned} p_x &= s_x + \sin \tau \cdot r \\ p_y &= s_y \pm (r^2 \cdot \cos^2 \tau - s_z^2)^{1/2} \end{aligned} \quad (30)$$

Equation (30) can easily be verified from Figure 11.

3.2 Computation of ground coordinate from given image coordinates when the exterior orientation is not known

An unknown exterior orientation leads to the necessity of using control points or—more generally—control information to relate image and object space. This has been attempted by many authors. The efforts can be classified into:

- interpolative models employing so-called “rubber-sheeting” or warping algorithms to make the image fit to ground control;
- parametric models employing projection equations and computing unknown parameters from control point information; and
- hybrid combination of a) and b), where the projection equations are used to relate image and object, but where an interpolative technique is applied to represent unknown deviations of reality from the assumed model.

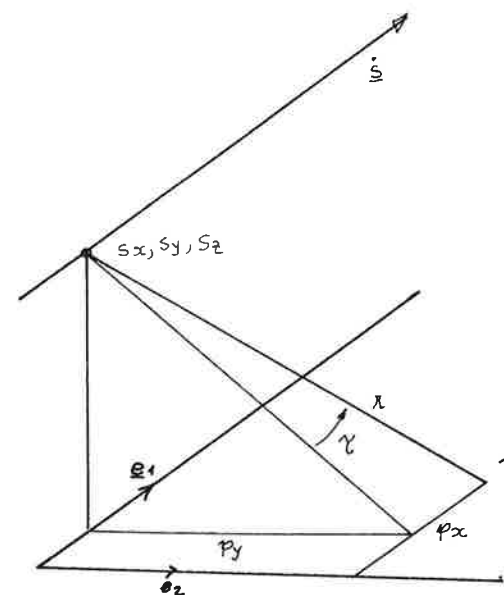


FIGURE 11 Simplified SLR geometry with specific exterior orientation.

3.2.1 *Interpolative methods* A first approach to the study of image geometry is to consider the image itself as a map substitute and to analyse its differences from a map of known geometric properties. Differences $\Delta x_i, \Delta y_i$ between image x_i, y_i and map X_i, Y_i coordinates can be measured at control points i . Some interpolation function is then used to predict $\Delta x_p, \Delta y_p$ deformations of the image at arbitrary image locations p . The same methods can be employed as those used in other photogrammetric interpolation tasks (Leberl, 1975). To give but two examples, let us consider Figure 12. The points $P_i, i = 1, \dots, n$ are known with their image coordinates x_i, y_i and map coordinates X_i, Y_i .

(a) Polynomials

We may now, as one example, attempt a scale fit:

$$\begin{bmatrix} X_i \\ Y_i \end{bmatrix} = \begin{bmatrix} a_{11} & a_{12} \\ -a_{12} & a_{11} \end{bmatrix} \begin{bmatrix} x_i \\ y_i \end{bmatrix} \quad (31)$$

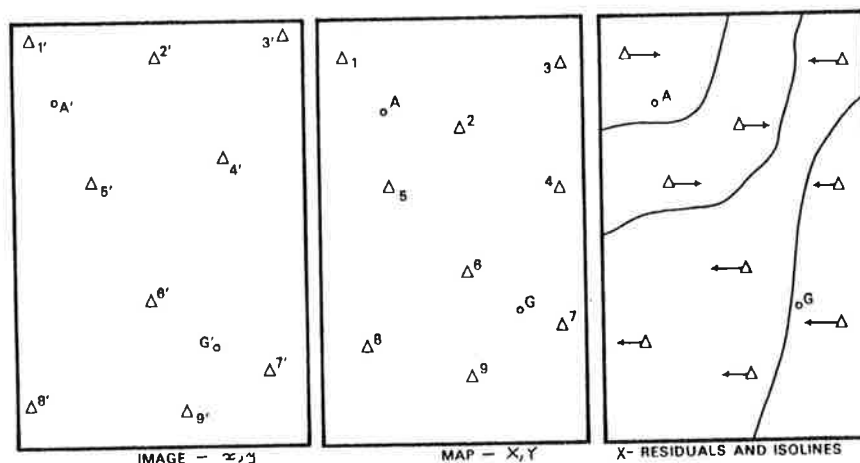


FIGURE 12 Interpolative method of relating image and map points; a preliminary transformation leads to residuals $\Delta X, \Delta Y$. These define a correction surface that can be described by isolines, separately for ΔX and for ΔY .

Since this is solved with more control points than needed one obtains residuals $\Delta X, \Delta Y$ or, if Eq. (31) is applied inversely, $\Delta x, \Delta y$. For a new point, x_p, y_p , we find thus first X_p', Y_p' and we obtain the final map coordinates by adding $\Delta X_p, \Delta Y_p$:

$$\begin{aligned} X_p &= X_p' + \Delta X_p \\ Y_p &= Y_p' + \Delta Y_p \end{aligned} \quad (32)$$

where $\Delta X_p, \Delta Y_p$ result from:

$$\begin{aligned} \Delta X_p &= a_0 + a_1 X_p + a_2 Y_p + a_3 X_p Y_p + a_4 Y_p^2 + \dots \\ \Delta Y_p &= b_0 + b_1 X_p + b_2 Y_p + b_3 X_p Y_p + b_4 X_p^2 + \dots \end{aligned} \quad (33)$$

The coefficients $a_0, \dots, a_n, b_0, \dots, b_n$ are computed from the known control point values $\Delta X_i, \Delta Y_i$.

Various authors have evaluated different types of polynomials for radar image correction (Leberl, 1970; Derenyi, 1974a; Hirsch and van Kuilenburg, 1976; Shakine and LeToan, 1978). A common conclusion is

difficult to draw, since different data from different sensors were employed. However, one may summarize that the use of polynomials is generally not advisable due to their predictably unfavourable behavior in the case of irregular control point distribution, and in the case of extrapolation. Polynomials are only recommended if they are of low order (1st or second) and if there is an even control point distribution.

(b) Moving average

The polynomials of Eq. (33) are a global, closed representation of image deformation. There are also point-wise methods of describing this deformation. We start from the known set of $\Delta X_i, \Delta Y_i$ -values in control points, and need to compute the $\Delta X_p, \Delta Y_p$ in a new point X_p, Y_p . The moving average technique assembles for each point P a set of known control points according to some criterion. This may for example be the n closest control points (Figure 13), or it may be m control points in each of four quadrants (Figure 14).

With these selected control point sets a polynomial of low order is now computed (1st or 2nd order) whereby each control point obtains a weight as a function of its distance from the new point. If all coordinates have

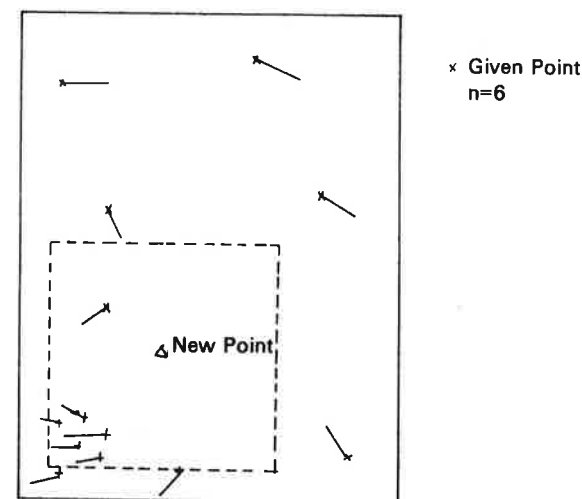


FIGURE 13 Moving average interpolation with square windows to collect n reference points.

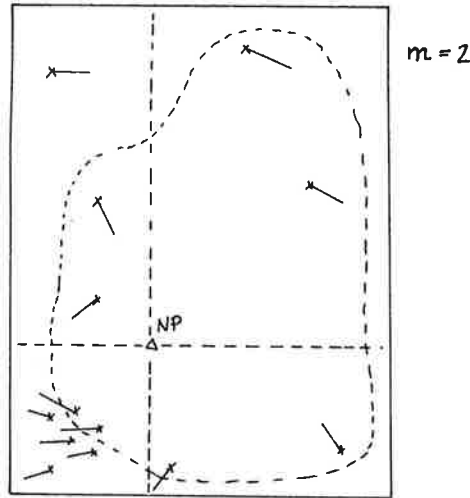


FIGURE 14 Selection of control points in quadrants, in this example with 2 points per quadrant.

been reduced to an origin in the new point, then only the first coefficients a_0, b_0 of this polynomial need to be computed:

$$\Delta X_p = a_0 + a_1 X_p' + \dots$$

$$\Delta Y_p = b_0 + b_1 Y_p' + \dots$$

since $X_p', Y_p' = 0$.

This computation and control point selection is repeated for each new point. In the case of a first order polynomial one also has the expression "moving plane" interpolation. A zero-order polynomial leads to a simple weighted average interpolation.

3.2.2 Parametric models The exterior orientation of the sensor is a function of time and therefore continuously changing. As a result each image- x -coordinate relates to a different exterior orientation. It is obvious that there cannot be a rigorous reconstruction of the exterior orientation from control points for all times t : the number of unknown exterior orientation elements is infinite. Even if we had several control points imaged at one given time t and thus along one line in the image- y -

direction, complete computation of the exterior orientation is not possible.

To illustrate the problem let us assume that the exterior orientation is nearly perfect and that the flight only slightly deviates from a straight line along the object e_1 -coordinate axis. Also ϕ, ω, κ , the elements of the sensor attitude, are nearly zero.

These small deviations $d\phi, d\omega, d\kappa, ds_x, ds_y$, and ds_z of the sensor from a predictable exterior orientation can be related to image coordinate errors dr, dt , or dx, dy . We start from Eqs. (11) and (12):

$$\bar{p} = \underline{A}^{-1} \cdot (\underline{p} - \underline{s}) \quad (34)$$

Differentiation of Eq. (34) leads to:

$$d\bar{p} = d\underline{A}^{-1}(\underline{p} - \underline{s}) - \underline{A}^{-1} \cdot d\underline{s} \quad (35)$$

where $d\underline{s} = (ds_x, ds_y, ds_z)$. Since we assume $\phi = \omega = \kappa \approx 0$, we get \underline{A}^{-1} to be the unit matrix, \underline{E} .

The differential form $d\underline{A}^{-1} \cdot (\underline{p} - \underline{s})$ is well known in photogrammetry (Rinner and Burkhardt, 1972):

$$d\underline{A}^{-1} \cdot (\underline{p} - \underline{s}) = \begin{bmatrix} 0 & -d\kappa & d\phi \\ d\kappa & 0 & -d\omega \\ -d\phi & d\omega & 0 \end{bmatrix} \underline{A}^{-1}(\underline{p} - \underline{s}) \quad (36)$$

Therefore we get with $\underline{A}^{-1} \cdot (\underline{p} - \underline{s}) = (u_p, v_p, w_p)^T$:

$$\begin{bmatrix} du_p \\ dv_p \\ dw_p \end{bmatrix} = \begin{bmatrix} -d\kappa \cdot v_p + d\phi \cdot w_p - ds_x \\ d\kappa \cdot u_p - d\omega \cdot w_p - ds_y \\ -d\phi \cdot u_p + d\omega \cdot v_p - ds_z \end{bmatrix} \quad (37)$$

Errors of image x, y -coordinates result from du_p, dv_p and dw_p as follows:

$$dx = du_p$$

But $y = r = (v_p^2 + w_p^2)^{1/2}$. Therefore:

$$\begin{aligned}
 dy &= dr = \frac{1}{r} (v_p \cdot dv_p + w_p \cdot dw_p) \\
 &= \sin \Omega \cdot dv_p - \cos \Omega \cdot dw_p
 \end{aligned}$$

Let us now simplify further with squint angle $\tau=0$. Then $u_p=0$, $v_p=r \sin \Omega$ and $w_p=-r \cos \Omega$. Thus

$$\begin{aligned}
 dy &= \sin \Omega (-d\omega \cdot w_p - ds_y) - \cos \Omega (d\omega \cdot v_p - ds_z) \\
 dy &= +d\omega \sin \Omega \cdot r \cdot \cos \Omega - \sin \Omega ds_y \\
 &\quad - \cos \Omega d\omega \cdot r \cdot \sin \Omega + \cos \Omega ds_z \\
 dy &= -\sin \Omega ds_y + \cos \Omega ds_z \\
 dx &= -r \sin \Omega d\kappa - r \cdot \cos \Omega d\phi - ds_x
 \end{aligned} \tag{38a}$$

With flying height $H=r \cdot \cos \Omega$, or with object coordinates $p_y=r \cdot \sin \Omega$, this can be rewritten:

$$\begin{aligned}
 dx &= -ds_x + p_y \cdot d\kappa - H \cdot d\phi \\
 dy &= -p_y/r ds_y + H/r ds_z
 \end{aligned} \tag{38b}$$

We see again that we have only five elements of exterior orientation. The sixth element, $d\omega$, has no effect on image geometry.

For each image-x-coordinate, a complete set of five orientation elements must be solved. This is not possible with a co-linear arrangement of control points, since clearly the effects of ds_x and $d\phi$ cannot be separated. We can solve either $(ds_x, ds_y, ds_z, d\kappa)$ or $(d\phi, ds_y, ds_z, d\kappa)$. The fifth element must be known. The required number of control points to compute the four elements is two.

It is unrealistic, however, to assume that for each image x-line one can have two control points. Also this is not necessary because of correlation that exists between the exterior orientation values at two different times t_1 and t_2 .

Authors have in the past proposed various mathematical models for the exterior orientation as a function of time, e.g. DBA-Systems (1974)

employed polynomials such that:

$$\begin{aligned}
 d\phi(t) &= a_0 + a_1 t + a_2 t^2 + \dots \\
 ds_z(t) &= f_0 + f_1 t + f_2 t^2 + \dots
 \end{aligned} \tag{39}$$

Instead of solving $d\phi$, $d\kappa$, ds_x , ds_y and ds_z one solves for unknown polynomial coefficients $a_0, a_1, \dots, f_0, f_1, \dots$. Eq. (38) is thus rewritten:

$$\begin{aligned}
 dx &= -\{c_0 + c_1 t + c_2 t^2 + \dots\} \\
 &\quad + p_y \cdot \{b_0 + b_1 t + b_2 t^2 + \dots\} \\
 &\quad - H \cdot \{a_0 + a_1 t + a_2 t^2 + \dots\} \\
 dy &= -\frac{p_y}{r} \cdot \{d_0 + d_1 t + d_2 t^2 + \dots\} \\
 &\quad + \frac{H}{r} \cdot \{e_0 + e_1 t + e_2 t^2 + \dots\}
 \end{aligned} \tag{40}$$

Not all coefficients can be determined separately. The analysis of this approach is beyond the scope of this paper. It may, however, be relevant to point out that instead of single high order polynomials it is preferable to use piecewise polynomials of low order. Baker and Mikhail (1974) have studied these approaches, however, for aircraft scanner imagery, not for radar.

Dowideit (1977) studied the method of modelling the exterior orientation parameters by Fourier series, correctly arguing that the elements of the exterior orientation have a periodical behavior with several dominating frequencies (Leberl, 1972a). Again, one has to solve for unknown coefficients of the Fourier series. The main problem is instability of the resulting equation system due to correlation among coefficients.

A somewhat different approach has been proposed for dynamic scanner images by Ebner and Hoessler (1978). The elements of exterior orientation are considered to form time-series appropriately modelled by Gauss-Markoff-chains of order m :

$$\phi(t_{n+1}) = \sum_{i=1}^m a_i \phi(t_{n-m+i}) + \varepsilon_{n+1} \quad (41)$$

Thus the exterior orientation is described at discrete times t_1, t_2, \dots ; at time t_n , the orientation parameter is considered to be a linear extrapolation from m previous times plus a random addition, ε . Ebner and Hoessler could show that a numerically stable and comparatively manageable solution can be formulated. A detailed description is beyond the scope of this paper. An application to radar must still be investigated.

3.2.3 Hybrid methods A combination of parametric and interpolative methods is feasible and common in photogrammetry. A mathematically rigorous model of the imaging process, such as used in the parametric case, may not be able to describe the entire chain of physical events leading to the image. Unknown elements or effects must be considered. This can be done by introducing $\Delta x, \Delta y$ -corrections to the image coordinates; these corrections can be represented by polynomials or other interpolative methods.

In photogrammetry this approach is denoted by "self-calibration", the concept is related to the method of so-called "collocation" (Moritz, 1973). An elementary implementation is by solving first a parametric formulation. This will be done in a least-squares method that leaves residuals at the observed image points. The residuals are then subject to an interpolative computation. This is meaningful only when the residuals form a systematic pattern such as shown in Figure 15. A new point $P(x_p, y_p)$ is thus converted to object coordinates by first adding $\Delta x_p, \Delta y_p$ to x_p, y_p , and by then applying the radar equations (22) to (30), respectively.

3.3 Computation of image coordinates for given ground points and with known exterior orientation

In the event that the exterior orientation is measured, e.g. with the help of inertial navigation, one must expect errors of measurement to exist. These require correction with the help of ground control points.

Figure 16 illustrates the solution to the computation of the image coordinates x, y for a given object point $P(p_x, p_y, p_z)$. The exterior orientation is known in the form of position vectors $\underline{s}_i, i = 1, \dots, m$ at

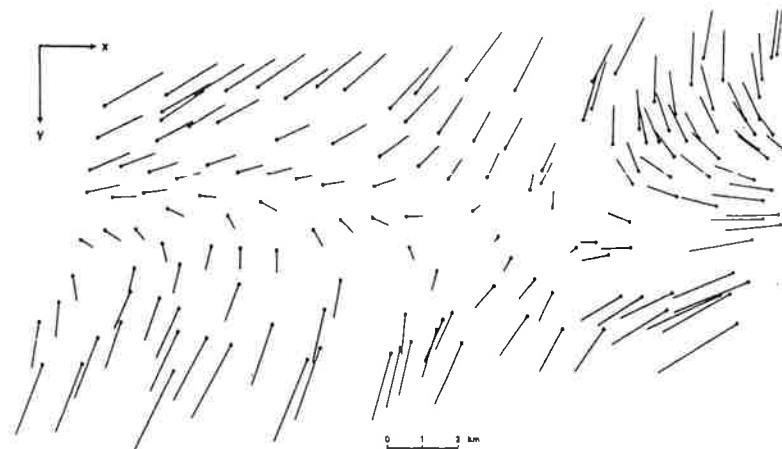


FIGURE 15 Example of a systematic pattern of image coordinate residuals. This belongs to the image and map of Figure 20.

times $t_i, i = 1, \dots, m$. Also given is thus the velocity vector $\dot{\underline{s}}_i = \underline{s}_{i+1} - \underline{s}_i$, or the equivalent attitude vector describing $\phi(t), \kappa(t)$.

From Figure 16 one finds:

$$(\underline{s}_i - \underline{p}) \cdot \dot{\underline{s}}_i = |\underline{s}_i - \underline{p}| \cdot |\dot{\underline{s}}_i| \cos \alpha_i$$

where α_i is the angle between the linear orbit element i and the vector from \underline{s}_i to \underline{p} . It relates to entity e_θ :

$$\cos \alpha = e_\theta / |\underline{s}_i - \underline{p}|$$

where e_θ results from:

$$(\underline{s}_i - \underline{p}) \cdot \dot{\underline{s}}_i = |\dot{\underline{s}}_i| \cdot e_\theta, \quad e_\theta = \dot{\underline{s}}_i \cdot (\underline{s}_i - \underline{p}) / |\dot{\underline{s}}_i|$$

With this we get orbit position \underline{s}_p :

$$\underline{s}_p = \underline{s}_i + \dot{\underline{s}}_i \cdot e_\theta / |\dot{\underline{s}}_i| \quad (42)$$

Position \underline{s}_p then leads to slant range r_p and time t_p of imaging:

$$r_p = (\underline{p} - \underline{s}_p) \quad (43a)$$

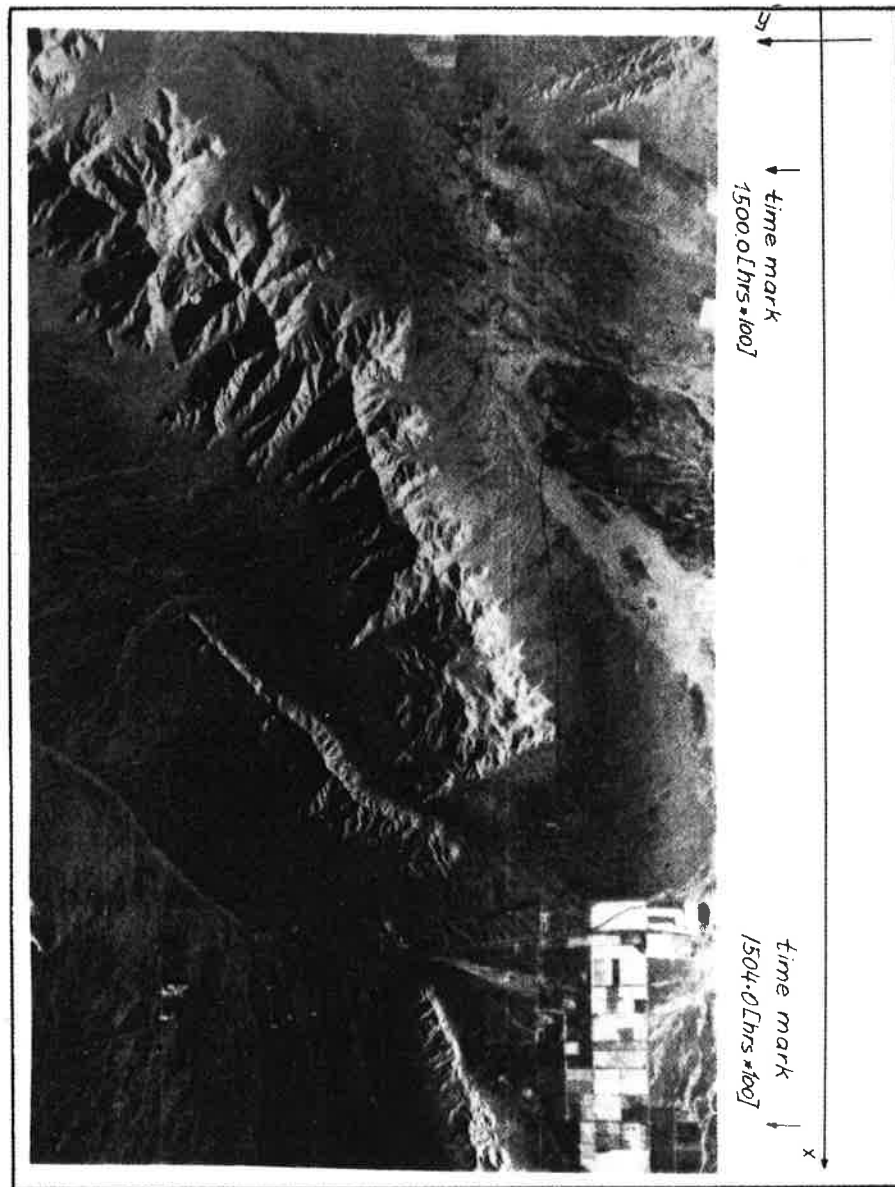
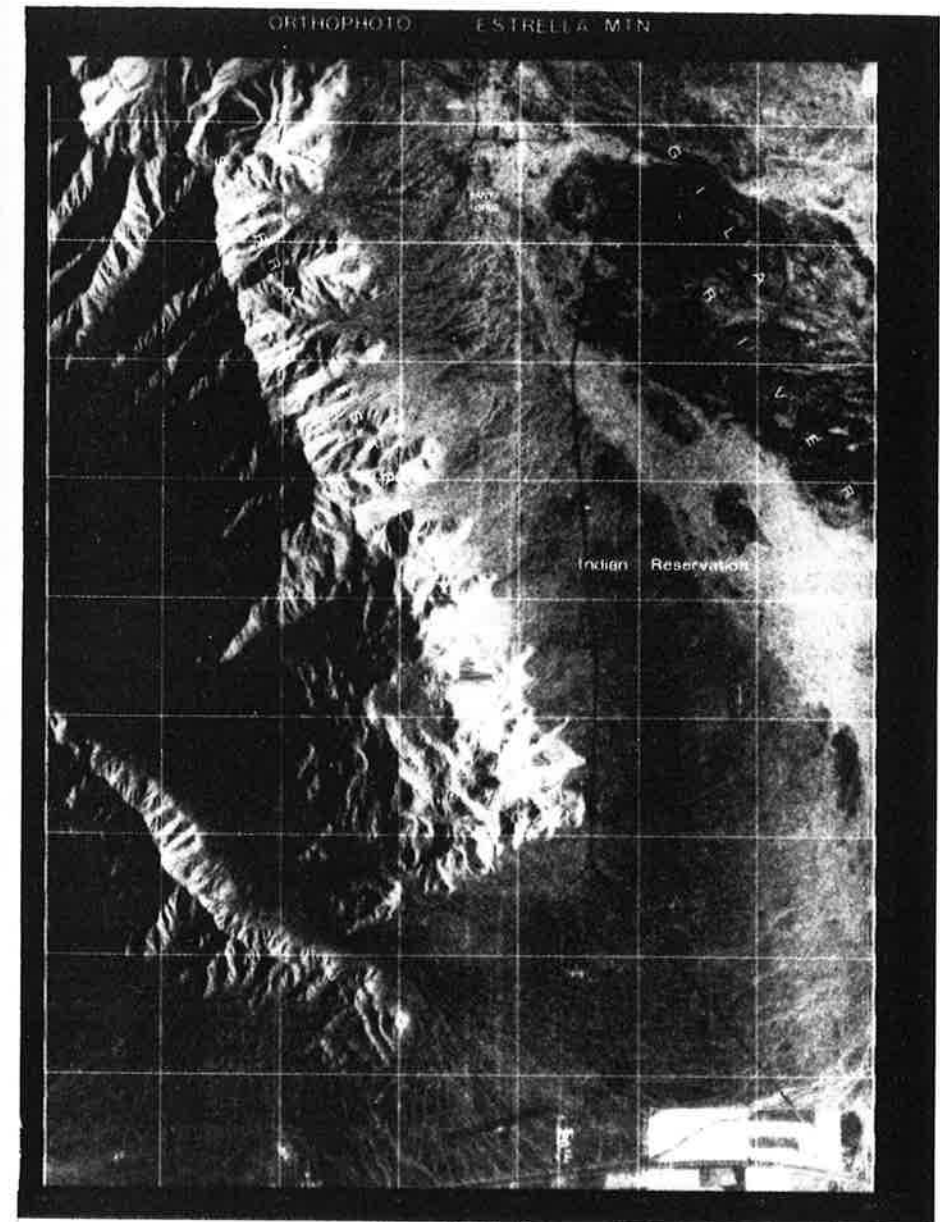


FIGURE 18 Original radar image (above) and orthophoto (opposite). Both from the Goodyear GEMS-system, flown at 12 km altitude over Estrella Mountains, Arizona, USA, using 3 cm wavelength.



radargrammetry. All image details inside a quadrangular grid mesh are transformed with a simpler and thus faster linear method.

The process is based on a raster DHM at orthophoto anchor points. These terrain points are resected onto the image according to Eqs. (42) to (45), so that a situation as shown in Figure 17 results. Based on these image coordinates one of the standard digital or analog photogrammetric rectification routines can be applied.

Figure 18 shows an original and a rectified aircraft radar image from a study by Leberl and Fuchs (1978). A 2 km UTM-grid is plotted over the radar ortho-image. The study by Leberl and Fuchs (1978) presented a detailed error analysis. Its discussion here would go beyond the scope of this paper.

Digital rectification has been done so far in the context of the SEASAT-mission. Curlander *et al.* (1981) have used digital SAR-images from SEASAT together with orbital data, and Naraghi *et al.* (1981) matched the SAR-data with a digital terrain model.

(b) Radar image mono plotting

Instead of actually creating a geometrically corrected radar image one can think of converting only certain interpreted image details to a map projection. If a DHM exists with the image and the image is related to the ground height through a computation of exterior orientation, then one can trace the image lines of interest with a digitizer; the image x, y -coordinates are transformed to X, Y knowing Z . This concept was realized by Greve and Cooney (1974) with radar, and is a method of photogrammetry which has also been proposed by other authors (e.g. Makarovic, 1973).

The idea has not yet had responses of any significance, either with metric photography or with radar or other image types. Interpretation of image contents apparently relies on the use of the stereo impression so that a pure single-image approach is not accepted even with existing DHMs.

3.5 Accuracies

(a) Theoretical prediction

Equations (35) and (38) related errors of exterior orientation to radar-image coordinate errors. The inverse relationship is of interest now, how

do errors of the inner and exterior orientation propagate into computed object coordinates?

Without an explicit derivation we only present the result of the analysis for the case of a slant range presentation:

$$dp_x = ds_x + H d\phi + p_y \cdot d\kappa$$

$$dp_y = ds_y + r/p_y \cdot dr - H/p_y \cdot ds_z \quad (44)$$

Figure 19 provides a graphical representation of this equation. From this it is obvious that the radargrammetrically computed ground coordinates p_x, p_y suffer particularly from erroneous ground or sensor height. Also the sensor attitude error causes changes of scale due to dependence of dp_y on p_y .

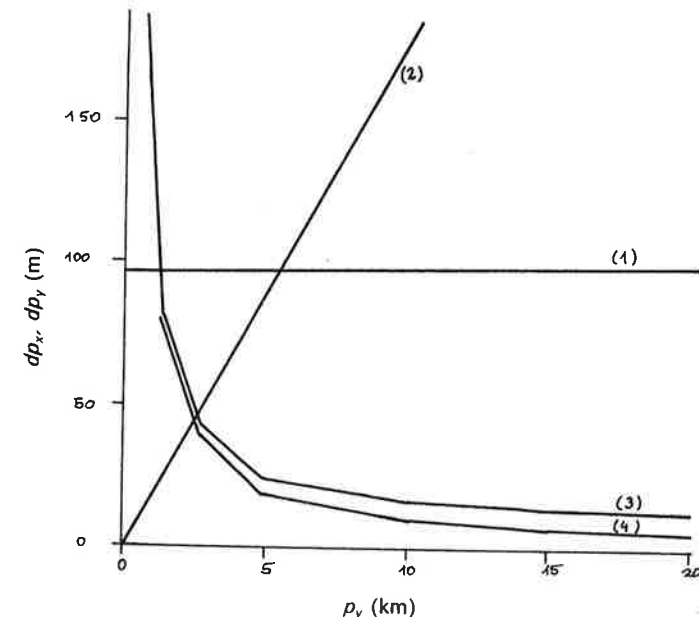


FIGURE 19 Errors of object coordinates as a result of errors of SLR exterior orientation, with $H = 10$ km. (1) dp_x due to $d\phi = 0.5^\circ$; (2) dp_x due to $d\kappa = 0.5^\circ$; (3) dp_y due to $dr = 10$ m; and (4) dp_y due to $ds_z = 10$ m.

(b) *Experimental results*

Numerous authors have compared single radar images to maps, thereby employing one of the described computing methods. An example of an early effort was by Leberl (1972a), as shown in Figure 20. Various interpolative methods were used to describe the image deformation.

Table I is a review of some existing work. In view of the many possible mapping methods, of variations in the image types, of input data available on the terrain etc., it is obvious that a comparison of results is nearly impossible. However, one conclusion can be drawn, the range of achievable results stretches from the geometric ground resolution (Gracie *et al.*, 1970) to some large figures. Clearly, though these larger figures may be caused by unknown topographic relief, lack of ground control points or poor internal geometry.

3.6 Some specific considerations regarding satellite radar

3.6.1 SEASAT-SAR theoretical accuracy prediction Using Eq. (44) for single image geometric error analysis of Section 3.4, we can plot curves for ground p_x, p_y -coordinate errors dp_x, dp_y as a function of errors of exterior orientation and of erroneous ground heights. Figure 21 illustrates some of these errors. It is demonstrated that the cross-track-coordinate p_y is affected by errors of either the sensor attitude or the ground height; along-track coordinates are a result of erroneous time measurements and of errors of the azimuth of the sensor velocity vector, \hat{s}_y .

When considering the satellite radar image as a map substitute we need to understand geometric image errors due to numerous effects, expressed in the terms of map projection deformations according to Tissot (Leberl, 1978a). Not image points but image lines and areas are being considered and their deformation due to: planetary radius of curvature; Doppler cone; planetary rotation; orbit eccentricity; and meridional convergence. Such analyses were discussed by Leberl (1978a) but are beyond the scope of this paper.

3.6.2 SEASAT-SAR experimental accuracy Expectations were expressed in the preparation phase of satellite radar that it could result in higher image geometry performance than aircraft radar (Leberl, 1976b). SEASAT-SAR was the first data to potentially prove that expectation. However, the overall system engineering for SEASAT-SAR did not optimize geometric performance. Table II presents results obtained with

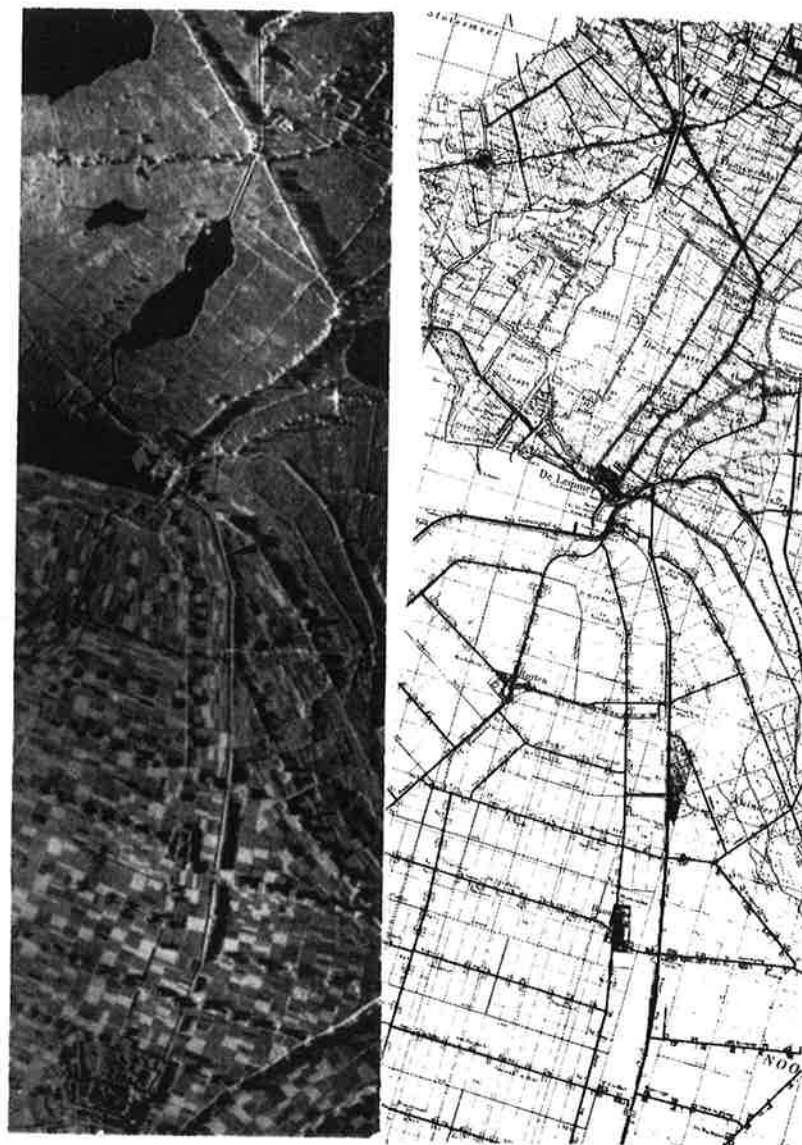


FIGURE 20 Example of a data set for an early single image accuracy evaluation. British real aperture radar flight (1965) over Noord-Oost-Polder, the Netherlands, and map at scale 1:50 000 for comparison.

TABLE I
Single image radargrammetric performance results (from Leberl, 1976b)

Source	Year	Accuracy (meters)		Relief	Control per 100 km ²	Resolution (ground-meters)	Antenna		Radar system code	Scale of images 1:	Area designation, remarks
		along 1σ	across 1σ				Stabilized	Type			
Gracie	1970	20	14	Flat	10.0	17	Yes	Synth.	AN-APQ 102	200 000	Atlanta, Georgia
Leberl	1971	50	23	Flat	10.0	30	No	Real	EMI (U.K.)	250 000	Netherlands
Bowman	1971	47	60	Flat	10.0	30	No	Real	EMI (U.K.)	250 000	Netherlands
Konecny	1972	152	255	Mount.		17	Yes	Real	Westinghouse	216 000	N. Guinea - conf transformation
Greve*	1974	35				≥3	Yes	Synth.	TOPO II	100 000	Dig. monoplottting
Goodyear	1974	38	30	Flat	3.0	12	Yes	Synth.	GEMS 1000	400 000	Phoenix, Arizona
Derenyi	1974	89	111	Hills	1.1	17	Yes	Real	Westinghouse	250 000	Washington, D.C.
DBA-Systems*	1974	51	26		0.5	3	Yes	Synth.	AN-ASQ 142	100 000	Radar interferometer
Konecny	1975	80	79	Flat		12	Yes	Synth.	GEMS 1000	400 000	Phoenix - conf transformation
Derenyi	1975	30	28	Flat		12	Yes	Synth.	GEMS 1000	400 000	Phoenix - control density not spec
Tiernan**	1976	209	257	Flat	0.7	30-150	No	Synth.	Apollo 17	1 Mill.	Lunar satellite
Leberl**	1976	147	233	Flat	0.3	30-150	No	Synth.	Apollo 17	1 Mill.	Lunar satellite
Hirsch	1976	120		Flat	3.0	30	No	Real	EMI (U.K.)	100 000	Netherlands
Leberl	1976	140	190	Flat	0.3	25-150	No	Synth.	JPL L-band	500 000	Alaskan tundra - sat. radar simul.

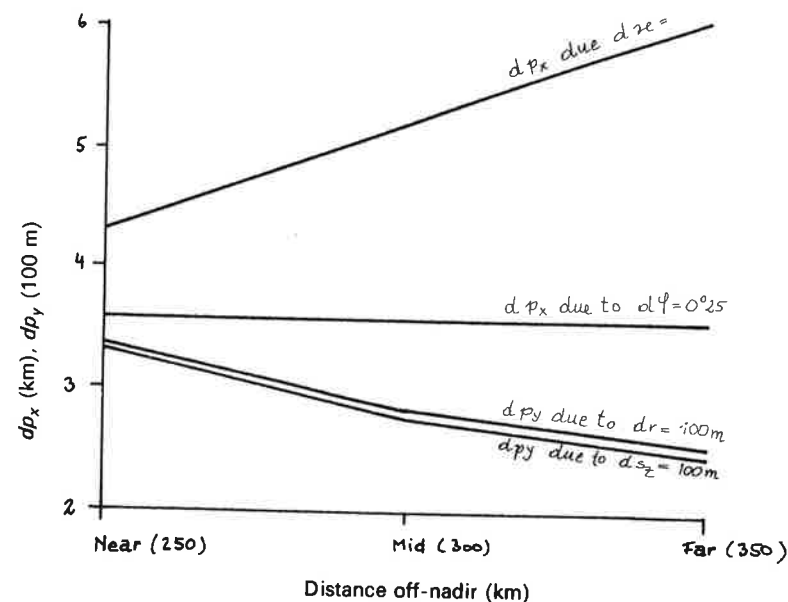


FIGURE 21 Effects dp_x , dp_y of ds_z , $d\phi$, $d\kappa$, dr on SEASAT-SAR.

TABLE II
SEASAT-SAR geometric accuracy. Coordinate errors in km after radargrammetric measurements and computation, using the arctic passes over Banks and Victoria Islands taken by SEASAT covering 35 000 km², and pass 351 over Los Angeles

No. of control points	Rigorous radar-grammetry		Simple scale fit	
	x	y	x	y
Sea arctic images of Banks Island, 35 000 sq km				
1	0.45	0.49	—	—
2 (at both ends)	0.33	0.26	0.37	0.37
17	0.17	0.16	—	—
Image over Los Angeles, 7 pts per 100 sq km				
Optical corr.	0.024	0.017	—	—
Digital corr.	0.022	0.012	—	—

SEASAT-SAR. Hardcopy images on film either from optical or from digital correlation provided the same accuracy. Time and range referencing was not of sufficient quality to fully capitalize on a relatively stable orbit geometry and the resulting good geometric potential (Leberl *et al.*, 1981). Without any ground control no meaningful positioning of ground points was feasible. With one or two such points the positioning error is ± 300 to 400 m.

The rigorous use of digital imagery enables one to more fully exploit the data geometrically (Brown *et al.*, 1981). Each pixel can be associated with a precise sensor events time and a slant range between antenna and object. As a result the location of an object on the Earth's surface can be computed without any ground control point to within several hundreds of meters. For the case of SEASAT, there is thus little difference between the use of rigorous radargrammetry and coarse approximations, except for the total lack of ground control or the presence of merely one or two points. For more appropriate mapping applicability a satellite radar would have to be equipped with precise time and range references and would need to be accompanied by accurate satellite orbit data with errors smaller than the geometric resolution of the sensor.

3.6.3 Applications to sea-ice mapping Single satellite radar images of SEASAT have been used to establish measurements of sea-ice motion. For this purpose a sequence of repetitive single image passes were

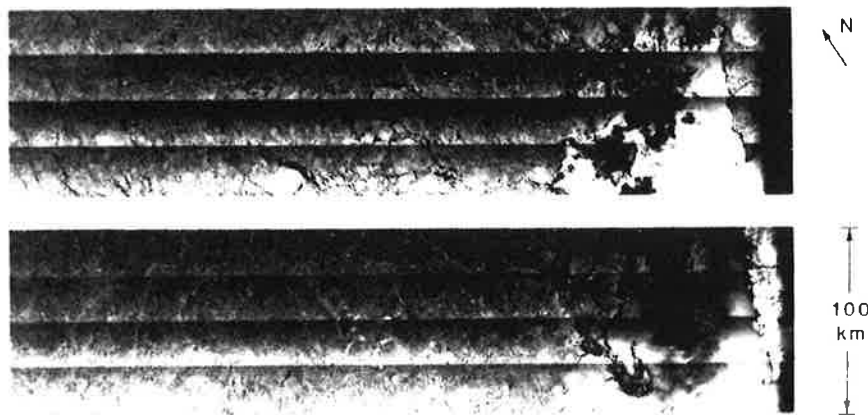


FIGURE 22 Example of SEASAT-SAR sea-ice images over Beaufort Sea, northwest of Banks Island, Canada, orbits 1339 (above), 1382 (below) (courtesy NASA-JPL).

generated by the SEASAT-experiment over the Beaufort Sea (Leberl *et al.*, 1981). Figure 22 shows an image pair taken three days apart, Figure 23 illustrates the changes of a specific section of the ice sheet over a period of one month.

Applying rigorous radargrammetry one can map the same ice features from sequential images and thereby derive sea-ice motion. Figure 24 shows the result and points to the potential usefulness of an all-weather sea-ice monitoring capability. SEASAT-SAR, however, did not exist long enough to enable development of more than a sequential single image approach. Challenges still remain to create systems employing blocks of adjoining image strips covering large areas, and to operate with all-digital image data. These concepts will certainly be realized when a more operational satellite radar becomes available.

4 PLOTTING FROM RADAR STEREO MODELS

4.1 General

Stereo viewing of overlapping images is a valuable tool in photo-interpretation. It is also an indispensable technique to identify homologue image points for measurement of image coordinates and reconstruction of a three-dimensional model. This may serve to create a model of terrain topography, such as in the form of contours, or to selectively measure slopes and relative height differences.

Stereoscopy refers to a visual perception of an overlapping image pair by an observer. A three-dimensional model is formed in the observer's brain. Also the computational process of generating 3-dimensional object coordinates from monocular image measurements is sometimes called "stereo", more correctly "stereology".

For the observer radar stereo is not different from its photographic equivalent. However, there is an entirely different mathematical model. The human operator perceives relief displacement in the form of so-called parallax differences, just as is the case in natural binocular vision (Figure 25a). It is the simulation of this binocular vision by presentation of two images to the eyes that is called stereoscopic viewing (Figure 25b).

There is a considerable body of literature on stereo perception. A recent review is by La Prade *et al.* (1980). Some basic facts may be worth presenting also in the current context. The minimum retinal disparity for binocular vision to be observable is 3" to 20", where the optimum is

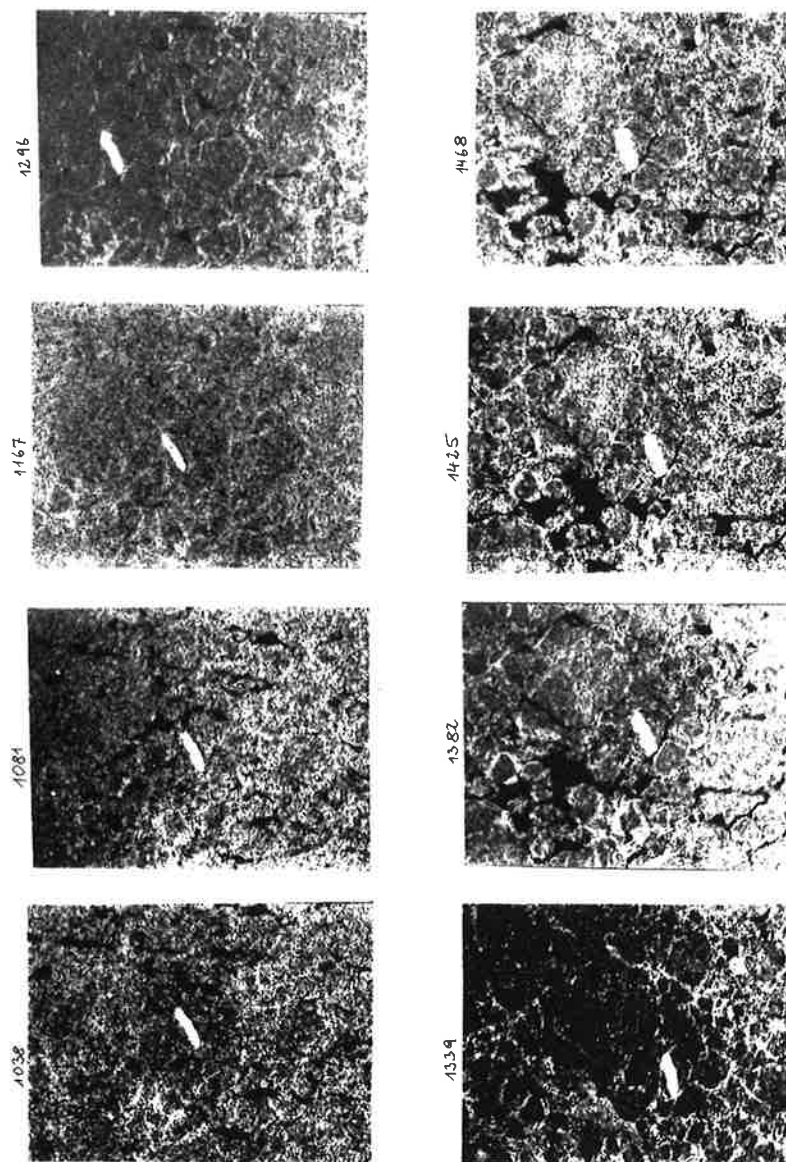


FIGURE 23 Changes of the ice as seen by SEASAT-SAR during a period of one month, between orbit 1038 (day 250 of 1978), and orbit 1468 (day 280 of 1978).

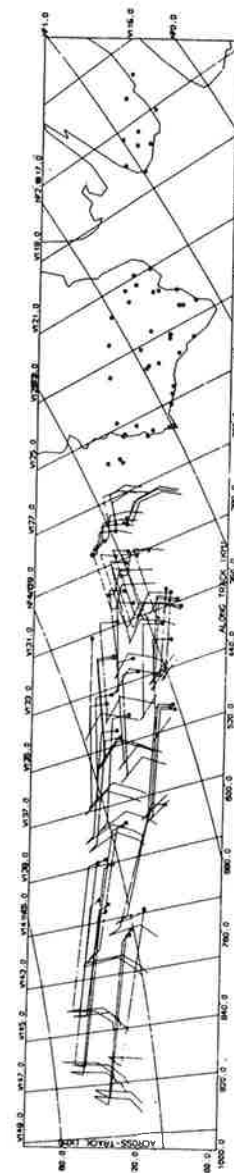


FIGURE 24 Sea-ice motion obtained from 7 SEASAT-SAR images between day 250 and 280 of 1978 over the Beaufort Sea.

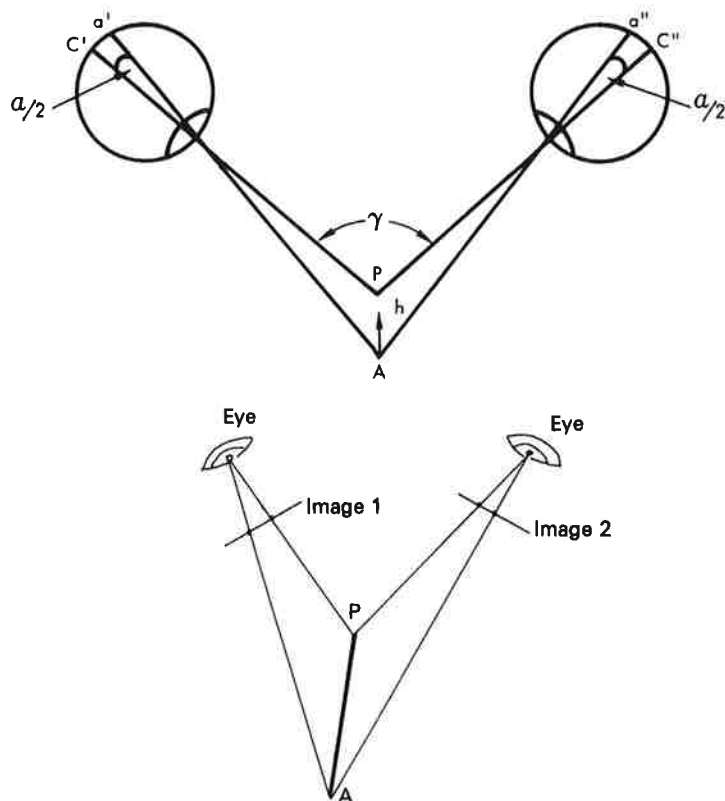


FIGURE 25 (a) Binocular vision and angular disparity; and (b) Stereoscopic viewing (from La Prade *et al.*, 1980).

attainable with parallel lines. Monocularly two objects can be distinguished if they create an angular disparity in one eye of more than $20''$. It is thus clear that stereo has a distinct advantage already from this point of view: if we were to monocularly measure the same point in two images, a measuring error will be committed in excess of $20''$.

An evaluation of stereo viewability and quality is possible using a vertical exaggeration factor, q . This is related to central perspective geometry which is the model of human vision. Figure 26 presents an observer looking at a stereoscopic image pair through the lenses of a stereoscope and the equivalent central perspective image collection geometry, illustrated for a pyramid-shaped object. The exaggeration

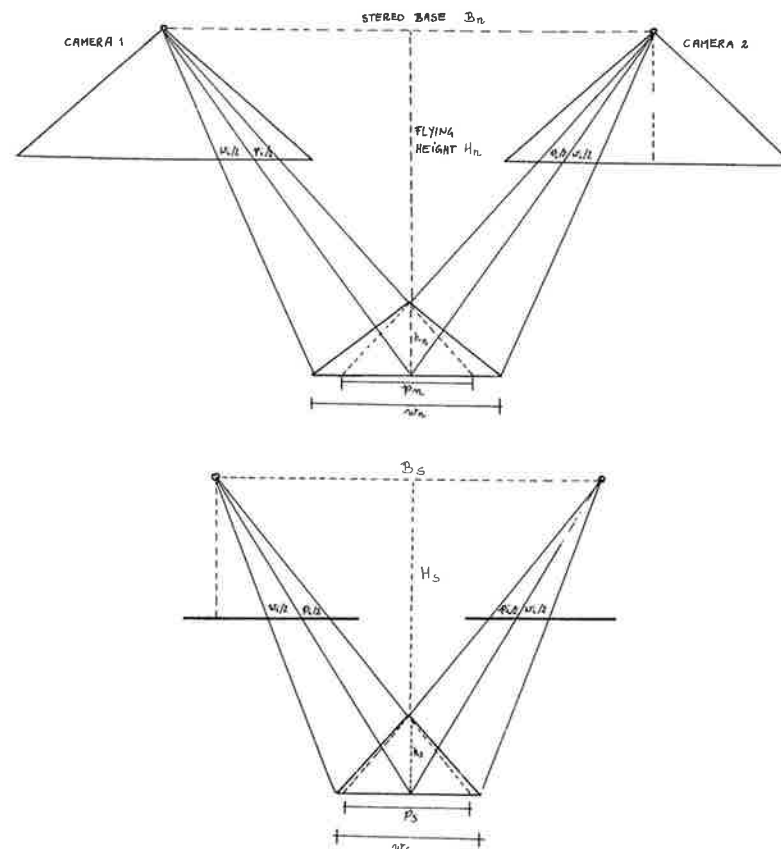


FIGURE 26 (a) Camera equivalent of stereo imaging an object of natural h_n/w_n dimension; and (b) stereoscope and vertical expression of the object with h_s/w_s (from La Prade *et al.*, 1980).

factor that is of relevance results from the ratio h/w of the pyramid as it is in nature (h_n/w_n) and as it appears from the stereo observation (h_s/w_s). This is thus a measure of the "flatness" of the subjectively observed stereo models.

In addition to the ratio in nature, h_n/w_n , and in the stereo-observation, h_s/w_s , there is the ratio in the image, p_i/w_i , according to Figure 26a, and the corresponding ratio in the object reference plane, p_n/w_n . We find:

$$p_n/w_n = p_i/w_i \quad (45)$$

$$p_n/h_n = B_n/H_n \quad (46)$$

where B_n is the equivalent camera stereo base and H_n the equivalent camera flying height. Thus:

$$p_i/w_i = (B_n/H_n)h_n/w_n \quad (47)$$

The stereoscopic observation has a stereo base, B_s , and distance to the virtual image, H_s . We find again from Figure 26:

$$h_s/p_s = H_s/B_s \quad (48)$$

$$p_s/w_s = p_i/w_i$$

Thus

$$h_s/w_s = (H_s/B_s)(p_i/w_i)$$

and

$$h_s/w_s = (H_s/B_s)(B_n/H_n)(h_n/w_n) \quad (49)$$

The vertical exaggeration, q , is then:

$$q = (h_s/w_s)/(h_n/w_n) \quad (50)$$

This is, for equivalent central perspective imaging:

$$q = (H_s/B_s)(B_n/H_n) \quad (51)$$

According to La Prade *et al.* (1980) optimum stereo viewing with a stereoscope requires the ratio H_s/B_s to be about 5. Section 4.5 will apply these relationships to radar images.

4.2 Radar stereo arrangements

The most commonly discussed radar stereo arrangements are illustrated in Figure 27 and are denoted by same-side and opposite-side stereo. La Prade (1963) was the first to propose stereo for side-looking radar. Numerous other authors addressed the topic of stereo, however mainly its computational aspects. Stereo viewability was studied by La Prade (1970), Graham (1975, 1976), Leberl (1978a, 1979). Computational aspects were treated by Innes (1964), Rosenfield (1968), Gracie *et al.* (1970),

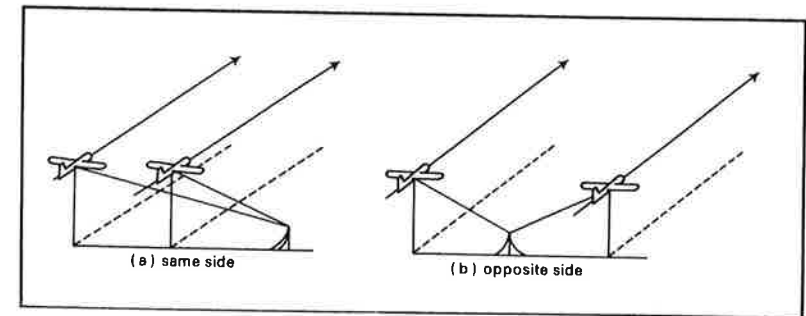


FIGURE 27 Same-side and opposite side radar stereo.

Konecny (1972), DBA-Systems (1974), Goodyear (1974), Derenyi (1975) and Leberl (1972, 1975c, 1978a).

Apart from the stereo cases of Figure 27 there have been proposals for cross-wise and other overlapping images from two flight lines (Leberl, 1972b; Graham, 1975) such as illustrated in Figure 28. For real aperture radar also single flight convergent schemes have been discussed by Leberl (1972b), Carlson (1973) and Bair and Carlson (1974, 1975). Single flight stereo cannot be obtained with synthetic aperture radar due to the fact that the projection line of a point is always a circle in a plane perpendicular to the flight line (velocity vector). A single flight line attempt to generate a SAR-stereo pair would fail due to the situation illustrated in Figure 29. In other words, the relief will always generate the same relief displacement, irrespective of the Doppler-frequency for correlation.

4.3 Radar stereo viewability

The two partners of a stereo image pair must be very similar in image quality or thematic content (tone, texture, etc.) so that they correlate well, whereas they should be sufficiently different in geometry to present parallaxes for height perception.

Radar is actively illuminating the object. Differences in geometry due to different sensor positions therefore imply also illumination differences. Good stereo from a geometric point of view therefore contradicts good viewability. In aerial photointerpretation the required parallaxes are obtained without any illumination differences in the two stereopartners; the sun illumination hardly changes from one photograph to the next.

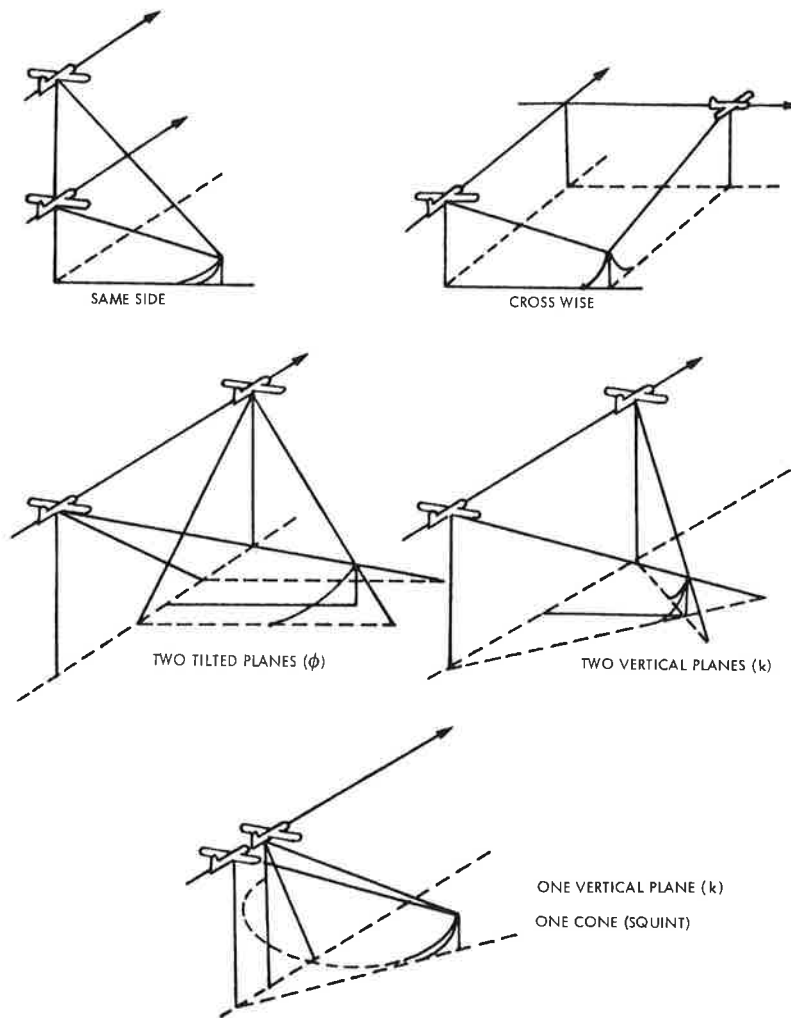


FIGURE 28 Radar stereo cases.

Stereo viewability is not a problem with photography. It is the essential problem with radar. Figures 30 through 36 present some examples of stereo radar models from: (i) aircraft at shallow look angles, with same-side illumination; (ii) aircraft at shallow look angles, with opposite-side illumination; (iii) aircraft with same-side illumination, and satellite

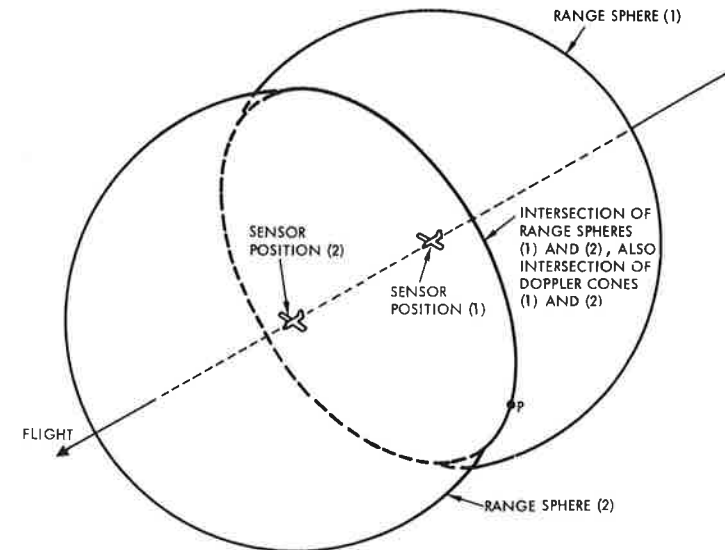


FIGURE 29 Single flight line stereo is not possible with SAR, the projection circles of the two images (forward and backward looking using positive and negative Doppler frequency for image correlation) will not intersect in a distinct point.

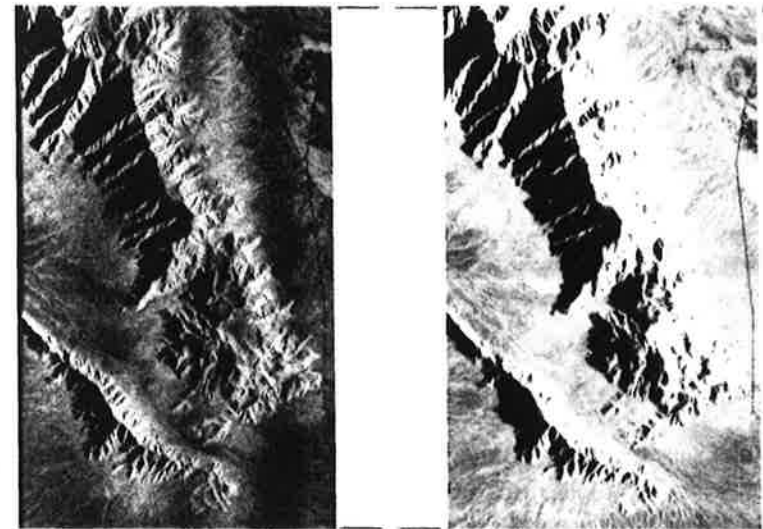


FIGURE 30 Same-side stereo pair of Estrella Mountain, Arizona (USA). SAR at 12 km altitude, 3 cm wavelength (courtesy Aero Service, Goodyear).

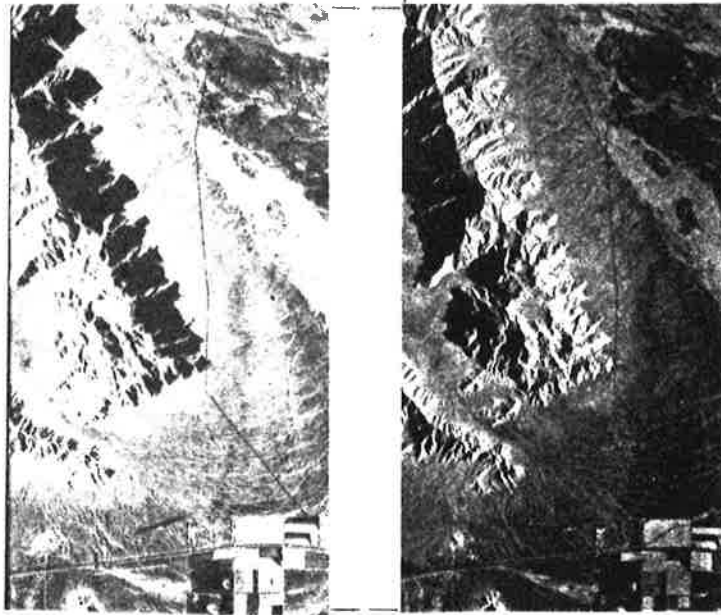


FIGURE 31 Same area as Figure 30, but with opposite side illumination.

SAR; (iv) satellite (SEASAT) with same-side illumination; (v) satellite (SEASAT) with opposite-side illumination; and (vi) lunar Apollo 17 radar with same-side illumination.

Table III reviews a set of stereo configurations with a subjective evaluation of viewability by an observer. The conclusion from the study of a larger set of radar stereo pairs is that influencing factors are: stereo arrangement; look-angles off-nadir; stereo intersection angles; and ruggedness of the imaged area.

Viewability is thus ensured at shallow look angles for same-side arrangements. Opposite-side stereo only is feasible with flat or gently rolling terrain. The limits of the actual performance are not yet well understood. One will have to investigate this with the help of a large variety of cases; image simulation offers a means to evaluate the subjective capabilities of an observer viewing radar stereo.

Le Prade (1975) reports on one experiment with operators studying same-side stereo of flat areas with man-made objects. Optimum results were reported to require look angles of 37° to 67° off-nadir, and

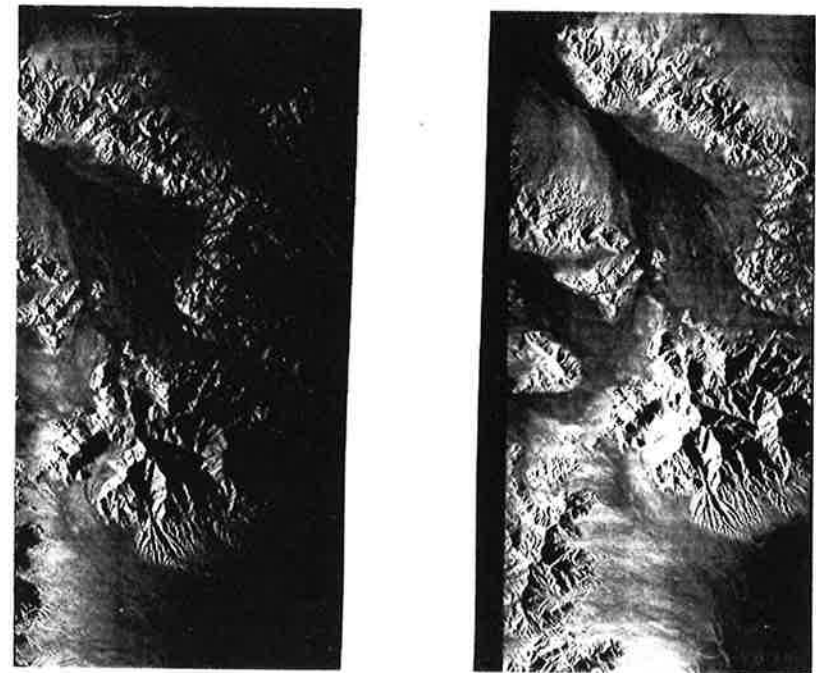


FIGURE 32 SAR-image pair of Granite Mountain, California (USA), from 12 km altitude, 3 cm wavelength (courtesy Aero Service, Goodyear).

intersection angles of about 12° to 15° . These intersection angles may seem poor, but it will be shown in Section 4.5 that radar has the potential to still produce vertical exaggeration factors approaching those of standard photointerpretation.

4.4 Radar stereo computations

(a) General case of stereo-intersection

A general formulation for radar stereo computations is based on Eq. (10), but for two overlapping images denoted by (') and (''):

$$\begin{aligned} p &= s' + r' \\ p &= s'' + r'' \end{aligned} \quad (52)$$

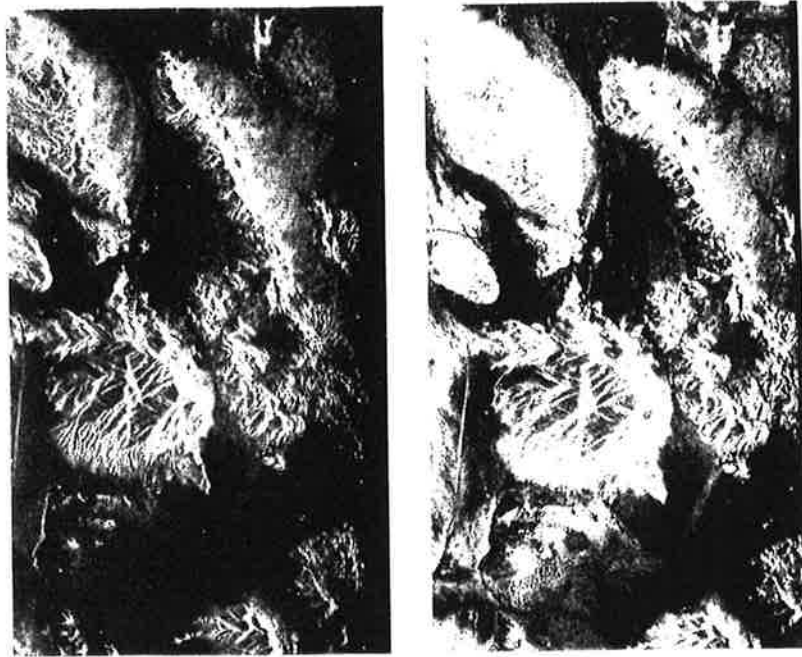


FIGURE 33 Same area as Figure 32, but from Seasat-satellite SAR, 25 cm wavelength.

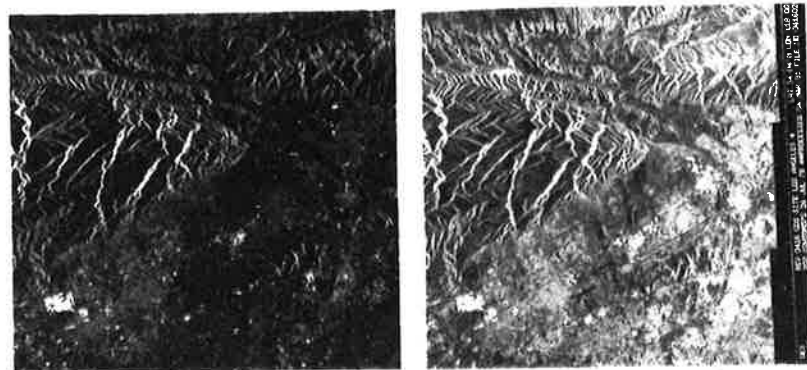


FIGURE 34 Same-side stereo of San Bernardino, California (USA), from Seasat-SAR.

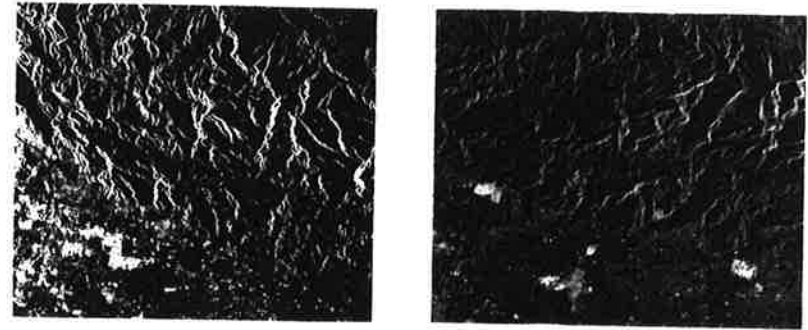


FIGURE 35 Opposite side stereo of part of Los Angeles. The imaged area overlaps partly with Figure 34.

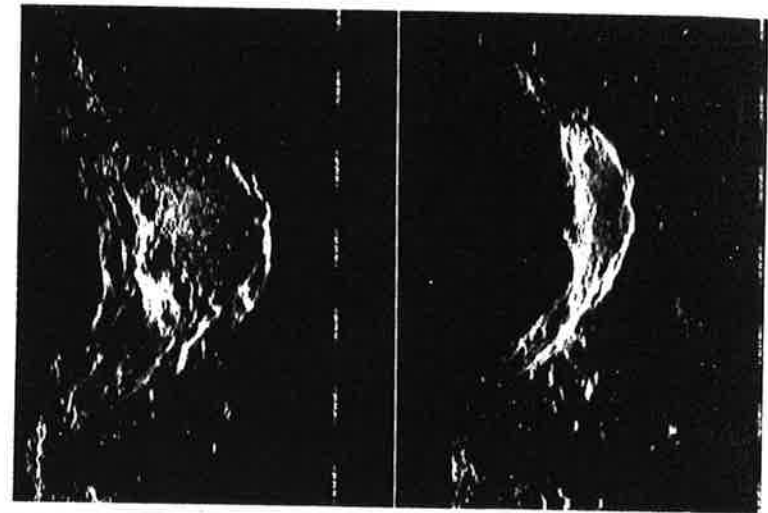


FIGURE 36 Lunar Apollo 17 same side stereo, 2 m wavelength: crater Buisson.

With the assumption of known interior orientation (conversion of image x, y -coordinates to time t and range r) as well as exterior orientation (sensor position \underline{s} , attitude or velocity vector $\underline{\dot{s}}$), expression (52) represents 6 scalar equations with 5 unknowns p_x, p_y, p_z, Ω' and Ω'' . We can eliminate \underline{p} from (52) to obtain a co-planarity equation:

$$\underline{s}' + \underline{r}' - \underline{s}'' - \underline{r}'' = 0 \quad (53)$$

which consists of 3 scalar equations with unknowns Ω' and Ω'' . An

TABLE III
Evaluation of viewability of a large number of stereo radar images

Type of radar	Number of models studied	Base length (km)	Look angle Ω'	Type of stereo	Intersection angle $\Delta\Omega$	Type of terrain	Stereo viewability
SEASAT-SAR	10	25-75	20°	Same-side	1°2-4°8	Rugged	Very convenient
Aircraft SAR	4	550	20°	Opposite-side	40°	Rugged	Not possible
Goodyear	2	0.7-13	68°	Same-side	0°2-23°	Rugged	Very convenient
Aircraft real aperture	1	30	68°	Opposite-side	120°	Flat to rugged	Only when flat
Motorola	1	10	81°	Same-side	6°	Flat to hilly	Convenient
Lunar Apollo 17 ALSE-SAR	1	48	80°	Opposite-side	160°	Flat to hilly	Convenient
	19	0.7-10.3	10°	Same-side	0°3-5°3	Flat	Convenient
						Rugged	Only with $\Delta\Omega < 1^\circ 9$

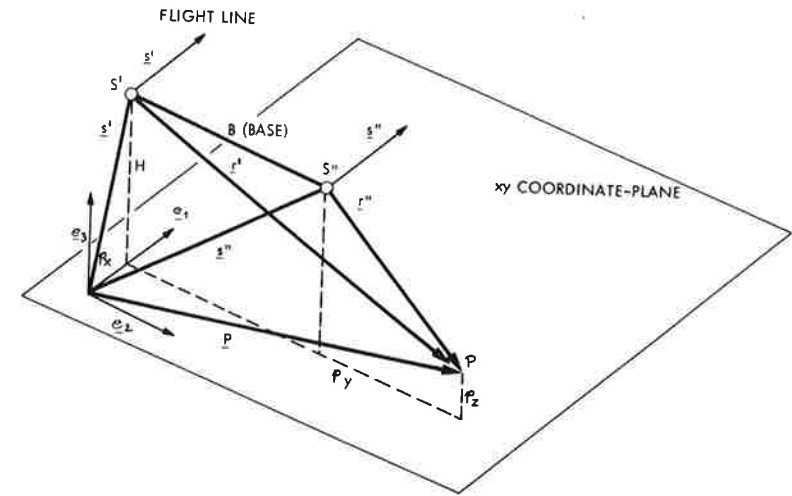


FIGURE 37 Simplified radar stereo case if flight line is parallel to the object- e_1 -coordinate direction.

alternative is to estimate r' , r'' :

$$|p - s'| = r'$$

$$|p - s''| = r''$$

$$\underline{s} \cdot (\underline{p} - \underline{s}') = \sin \tau' \cdot s' \cdot r'$$

$$\underline{s}'' \cdot (\underline{p} - \underline{s}'') = \sin \tau'' \cdot s'' \cdot r''$$

(54)

These are 4 non-linear equations with the three unknowns p_x , p_y and p_z . A solution is through linearisation and iteration.

(b) *Simplified case*

For a rectilinear flight at constant altitude we can find a simpler solution of the stereo intersection. Let us also assume that the flight is in a direction parallel to the object-x-coordinate axis (Figure 37). We obtain then:

$$\underline{s}' = (s_x, 0, H), \quad \underline{s}'' = (s_x, B, H)$$

$$\underline{s}' = (s_x, 0, 0), \quad \underline{s}'' = (s_x, 0, 0)$$

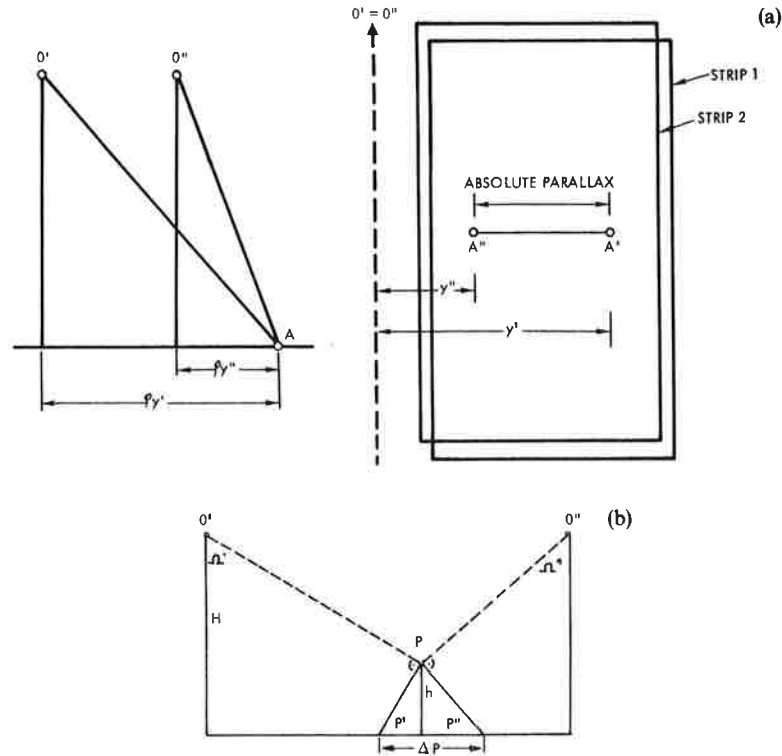


FIGURE 38 (a) Absolute parallax; and (b) parallax differences Δp due to a height difference h .

For squint angle $\tau = 0$ we then find from Eq. (54)

$$\begin{aligned}
 p_x &= (s_x) \\
 p_y &= (r'^2 - r''^2 + B^2)/(2B) \\
 p_z &= H - ((r'^2 - p_y^2)^{1/2} + (r''^2 - (B - p_y)^2)^{1/2})/2
 \end{aligned}
 \quad (55)$$

(c) *Simplified stereo computation with measured parallaxes*

Figure 38 defines absolute radar parallax and parallax differences; absolute parallax is measured when the flight lines of two images are

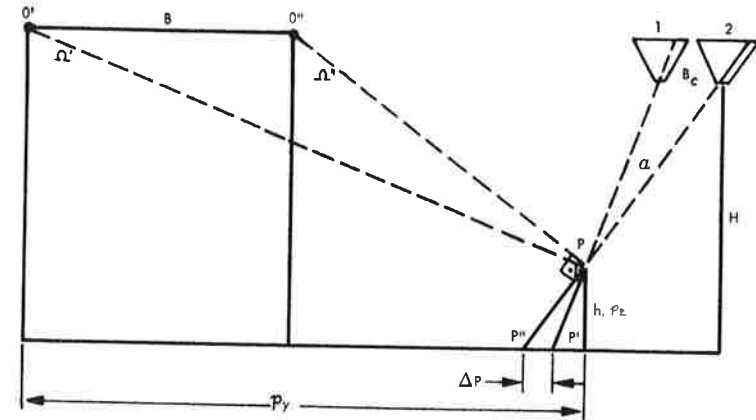


FIGURE 39 Relating an object height h to an observed parallax difference, Δp , in ground range presentation.

superimposed. Parallax differences are differences of absolute parallaxes between a given reference and a new point. We need to relate the object height above a reference datum to parallaxes measured in an image pair.

Rather than deriving an appropriate formula from Eq. (55) we read directly from Figure 39, replacing the actual projection circle by a tangent at the object point:

$$\begin{aligned}
 p' &= p_z \cot \Omega' \\
 p'' &= p_z \cot \Omega'' \\
 dp &= p'' \pm p' = p_z (\cot \Omega'' \pm \cot \Omega') \\
 p_z &= dp / (\cot \Omega'' \pm \cot \Omega')
 \end{aligned}
 \quad (56)$$

where the + sign applies to opposite and the - sign to same-side stereo.

An object height p_z can be computed if in addition to parallax difference dp one also knows the look angles Ω' and Ω'' . Clearly a given parallax difference dp generates different heights p_z , depending on Ω' and Ω'' . This is in contradiction to photographic stereo computation, where a given parallax difference relates to the same height, irrespective of where, in the stereo model, it has been measured.

Equation (56) applies to a ground range presentation as shown in

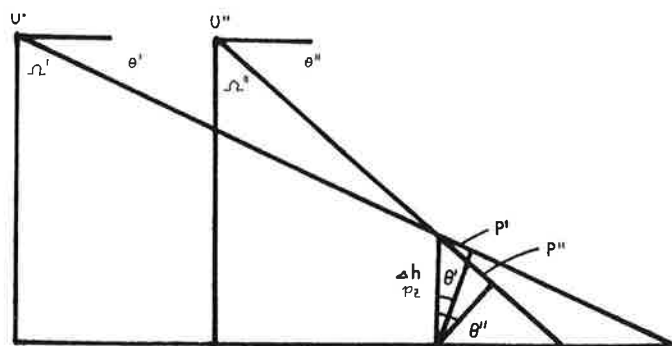
FIGURE 40 Parallax differences, $\Delta p = p'' - p'$, in slant range presentation.

Figure 39. In a slant range case, an observed parallax difference needs to be converted to a height p_z through a different formula. We have from Figure 40:

$$\begin{aligned} dp &= p' - p'' \\ p' &= p_z \cos \Omega' \\ p'' &= p_z \cos \Omega'' \\ p_z &= dp / (\cos \Omega' \pm \cos \Omega'') \end{aligned} \quad (57)$$

where + is for opposite- and - for same-side cases.

Again it must be stressed that Eqs. (56) and (57) are approximations only and are valid only for larger values of Ω' and Ω'' .

4.5 The visual appearance and vertical exaggeration of the stereo radar model

(a) Cylindrical deformation of slant range presentation stereo

Figure 41 is an explanation of why a slant range presentation image taken at steep look angles ($0^\circ < \Omega < 50^\circ$) makes the object appear on a cylindrical surface. Figure 41 is an explanation of this effect showing a bird's eye view which an observer has in the case of stereo models. An absolute parallax p is defined with slant range r' , r'' .

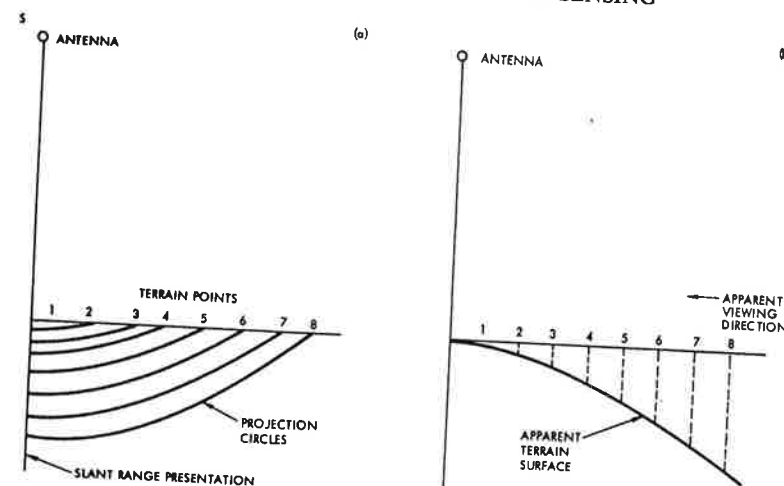


FIGURE 41 (a) A flat surface is projected along circles onto a projection plane through the antenna path. This is equivalent to an orthogonal projection as shown in (b), however, of a cylindrical surface. The imaged area appears cylindrical to an observer when in fact it is planar. Relief is shown as if it were on top of the cylinder (compare Figure 43).

$$p = r' - r''$$

so that

$$p = (H^2 + p_y^2)^{1/2} - (H^2 + (p_y - B)^2)^{1/2} \quad (58)$$

The absolute parallax p depends on the value of p_y . The relationship between p and p_y defines a "super-hyperbolic" cylinder in the space formed by a coordinate system with p_x, p_y, p (Leberl, 1978b). It is apparent that for $p_y = B/2$, $p = 0$; $p_y > B/2$ causes $p > 0$, and $p_y < B/2$ causes $p < 0$. The consequences are shown in Figure 42. An example of such an extremely deformed stereo model is shown as Figure 43. With ground range presentation this effect does not exist. It should, however, be clear that the parallax differences still cause deformations of heights, both in slant and ground range presentations. The result is discussed next.

(b) Quality evaluation using the vertical exaggeration factor q

An observer takes notice of parallax differences using the central perspective geometry associated with the eyes and the stereoscopic viewing equipment. This was discussed in Section 4.1. Parallax differences, dp , apparent in height differences, h , were related through the approximate relationship (56) for slant range presentation:

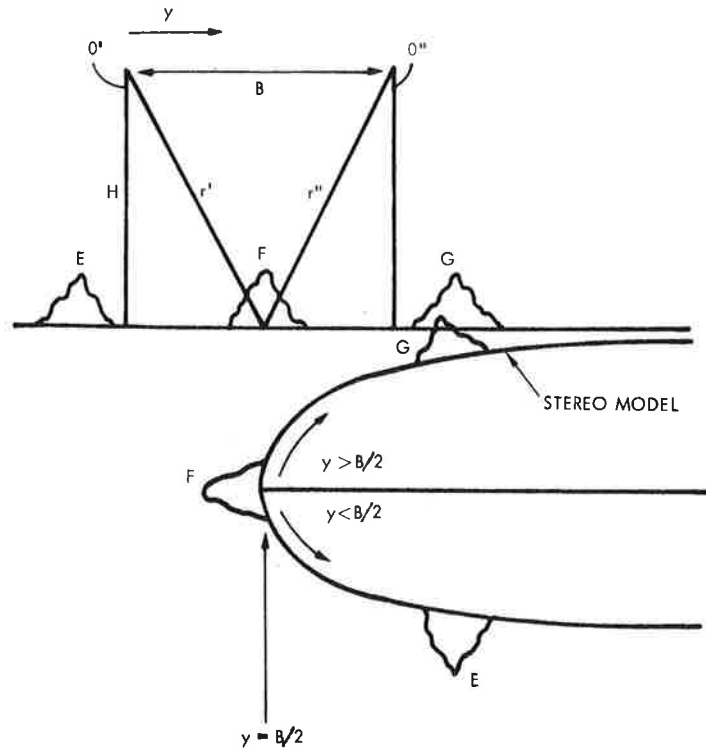


FIGURE 42 Slant range stereo causes a stereo model in which the terrain appears to be rolled onto a cylinder.

$$dp_i/h_i = \cot \Omega' - \cot \Omega'' \quad (56)$$

But in a central perspective viewing environment, dp_i/h_i in turn relates to an apparent (equivalent) camera stereo base, B_n , and flying height, according to Eq. (46):

$$dp_i/h_i = B_n/H_n \quad (46)$$

As a result we find:

$$B_n/H_n = \cot \Omega' - \cot \Omega'' \quad (59)$$

Introducing this into Eq. (51) and recalling that La Prade *et al.* (1980) have established optimum stereo viewing for $q \approx 5 \cdot B_n/H_n$, we find:

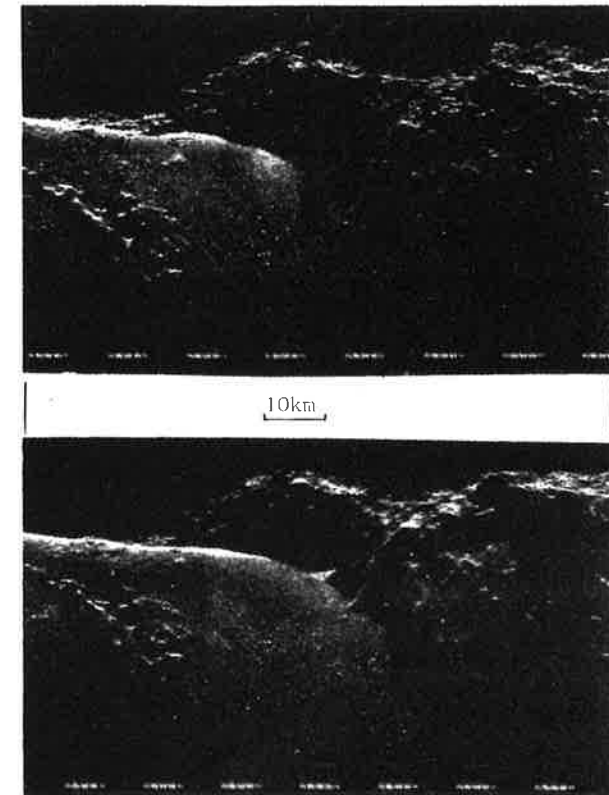


FIGURE 43 Example of a cylindrically deformed slant range stereo model, obtained on the Moon in the Apollo 17 mission (courtesy Jet Propulsion Laboratory, NASA).

$$q \approx 5 \cdot (\cot \Omega' - \cot \Omega'')$$

or, with reference to Figure 39:

$$q \approx 5 \cdot H_n \cdot B_n / (p_y(p_y - B_n)) \quad (60)$$

The range of Ω -values feasible for good radar viewing were discussed by La Prade (1975):

$$37^\circ < \Omega' < 67^\circ$$

$$12^\circ < \Omega' - \Omega'' < 15^\circ$$

TABLE IV
Vertical exaggeration factor with radar images shown in Figures 20-36

Area	Figure number	Type of radar	Look angle (°)	Intersection angle $\Delta\Omega$ (°)	Stereo base (km)	Exaggeration factor q
Estrella Mountain	30	Goodyear GEMS $\lambda = 3$ cm	68	10.9-19.2	14	1.2-1.9
Estrella Mountain	31	Goodyear GEMS $\lambda = 3$ cm	68	115	55	4.0
Granite Mountain	32	Goodyear GEMS $\lambda = 3$ cm	68	5.9-23.1	6	0.6-4.3
Granite Mountain	33	SEASAT-SAR $\lambda = 25$ cm	20	3.5	55	2.70 ^a
San Bernardino	34	SEASAT-SAR $\lambda = 25$ cm	20	3.1	50	2.43 ^a
Los Angeles	35	SEASAT-SAR $\lambda = 25$ cm	20	40	50	3.64 ^a
Moon	36	Apollo 17 ALSE $\lambda = 2$ m	10	5	10	9.7 ^a

^a For small look angles, the neglects made to derive the expression for q have an increasing effect.

Thus

$$2.3 > q > 1.8 \quad (61)$$

In stereo photography we have $B_n/H_n \approx 0.6$ to 1.0. Therefore we obtain $3 < q < 5$. Generally, then, radar stereo will tend to be poorer than photographic stereo with the above Ω -values.

While factor q is constant in a photographic case, it is variable with radar as shown in Eq. (60). The result is that a given parallax difference will create a more distinct vertical exaggeration at smaller values of Ω' or p_y .

Table IV describes the vertical exaggeration q in the images discussed in Section 4.3 and Table III. It is verified that successful stereo viewing of radar images is with data falling into a q -range as given by Eq. (61).

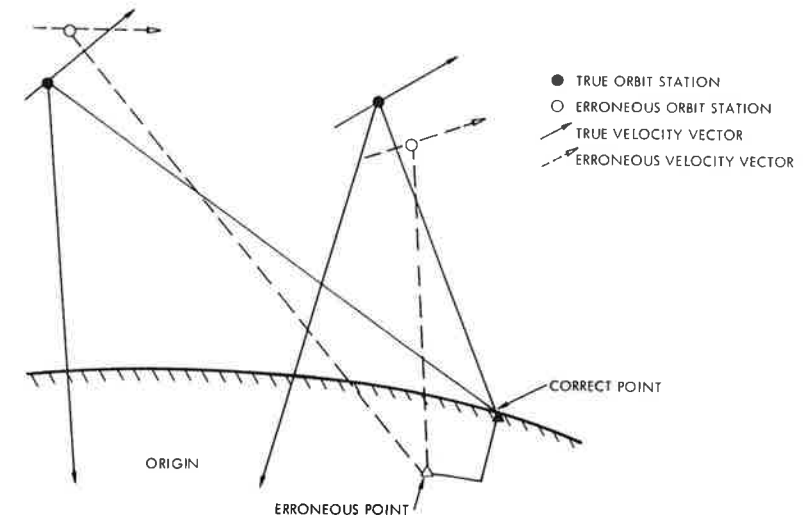


FIGURE 44 Concept of an absolute error of a stereo model point due to errors in the radar exterior orientation.

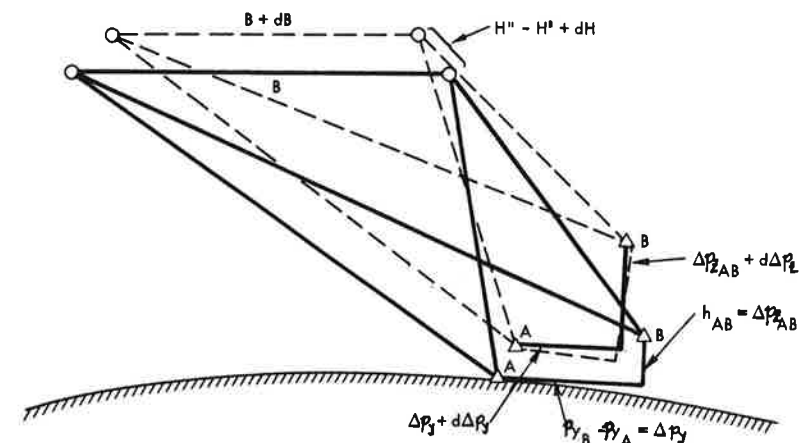


FIGURE 45 Concept of a relative error of stereo model distances due to erroneous exterior orientation.

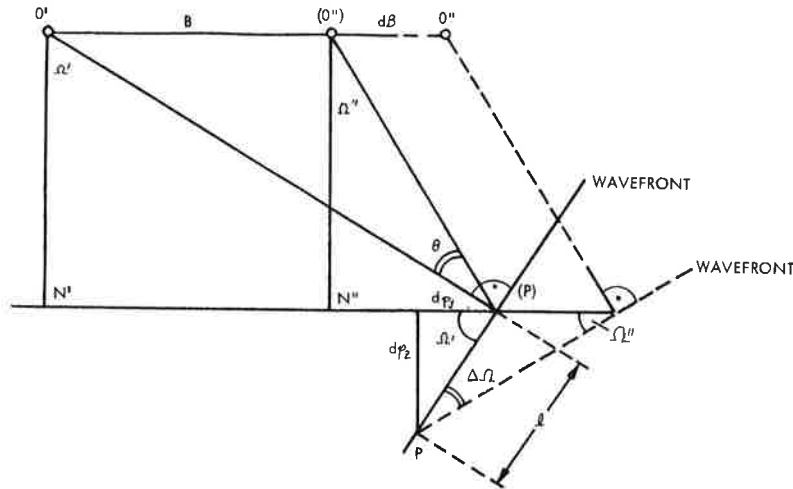


FIGURE 46 Analysis of the effect of an erroneous stereo base on the computed p_y, p_z -coordinates.

4.6 Analysis of radar stereo using error propagation modeling

Theoretical radar stereo error studies were performed by Rosenfield (1968), La Prade (1970) and Leberl (1972b, 1978a, 1979). They relate an error in an element of exterior orientation in the left or right image to the resulting error of the stereo model coordinates. One can carry this further to the errors of distances, height differences and angles etc. Figures 44 and 45 define the basic concept of the analysis.

A full description of the derivations of all error factors is beyond the scope of this review. The necessary material is, however, fully documented in an earlier report (Leberl, 1979). The method of analysis is illustrated for the example of the effect of an error in the stereo base, dB , on p_y and p_z -coordinates (Figure 46):

$$dp_y = l \cos \Omega'$$

$$dp_z = l \sin \Omega'$$

$$l = dB \sin \Omega'' / \sin(\Omega' - \Omega'')$$

Therefore

$$dp_y = (\cos \Omega' \sin \Omega'' / \sin(\Omega' - \Omega'')) \cdot dB$$

$$dp_z = (\sin \Omega' \sin \Omega'' / \sin(\Omega' - \Omega'')) \cdot dB \quad (62)$$

or

$$dp_y = ((B - p_y)/B) dB \quad (63)$$

$$dp_z = (p_y(p_y - B)/(H - B)) dB$$

Carrying this type of analysis through the various contributing elements we find:

$$dp_x = (ds'_x + ds''_x)/2 + p_y/2 \cdot d\kappa' + (p_y - B)/2 \cdot d\kappa'' + H/2(d\phi' + d\phi'') \quad (64a)$$

$$dp_y = (p_y/B) ds'_y + ((B - p_y)/B) ds''_y - H/B(ds'_z - ds''_z) + r'/B dr' - r''/B dr'' \quad (64b)$$

$$dp_z = (p_y(p_y - B)/HB)(ds'_y - ds''_y) + (B - p_y)/B ds'_z + p_y/B ds''_z + (r'(p_y - B)/(B \cdot H) dr' - (r'' \cdot p_y/BH) dr'') \quad (64c)$$

The errors of observed height differences between two points, $d\Delta p_z$, and of differences in cross-track distances, $d\Delta p_y$, result from the above (Leberl, 1979). Denoting $ds''_y - ds'_y$ by dB , error of stereo base, and $ds''_z - ds'_z$ by dH , difference of sensor altitude between the two images, we find:

$$d\Delta p_y = (-\Delta p_y/B) dB + (\Delta p_z/B) dH \quad (65a)$$

$$d\Delta p_z = \{((B - 2p_y)/(B \cdot H)\Delta p_y - (p_y(B - p_y)/(B \cdot H^2)) \cdot \Delta p_z\} dB + (\Delta p_y/B) dH \quad (65b)$$

The range resolution causes a random measuring error of range with mean zero and variances $\sigma_r'^2, \sigma_r''^2$. We find, from the last factors of Eqs. (64b and 64c) the following variances $\sigma_{p_y}^2, \sigma_{p_z}^2$, for cross-track and height coordinates:

$$\sigma_{p_y}^2 = \sigma_r'^2(r'^2 + r''^2)/B^2 \quad (66a)$$

$$\sigma_{p_z}^2 = \sigma_r'^2(p_y - B)^2 + r''^2 p_y^2 / (B^2 H^2) \quad (66b)$$

The analysis of the algebraic expressions (64), (65) and (66) are helpful

in appreciating the feasibilities and limitations of a specific stereo radar case, and to compute the effects of various parameters. Clearly the stereo model coordinates have errors that are different from those of distances and height differences. A sensor position error will be enlarged with factors p_y/B or H/B , thus with factors of 1 to 5. Sensor attitude errors ($d\phi$, dk or ds_y , ds_z) are comparatively irrelevant and affect essentially the along track coordinate, p_x . Throughout, an increase of the stereo base, B , improves the accuracy of the stereo model.

Range resolution limitations cause height errors that are smallest in the nadir, where p_y is zero, and increase with increasing p_y ; the cross-track coordinate is less accurate here than p_x . However, as p_y increases, the situation is reversed and p_y can be more accurate than p_x .

Height differences and cross-track distances are less affected by these errors than are coordinates themselves. To present but one example, assume a flight height H of 10 km, stereo base B of 8 km, $\Omega' \approx 68^\circ$ and $\Omega'' \approx 60^\circ$. An error of the stereo base, dB , of 100 m will alter the p_y -coordinate by 233 m, the p_x -coordinate by 577 m. But the same base error will affect an observed height difference of 1 km only by 50 m.

The essential limitations of stereo radar are caused by random range errors σ_r' , σ_r'' . In an aircraft stereo model of the above type errors will be caused by $\sigma_r = 10$ m with a σ_p of ± 42 m and with σ_p of ± 70 m.

Clearly satellite radar is less appropriate for stereo operations if the same look angle applies in both images; this leads to very small convergence angles $\Omega' - \Omega''$ or a small stereo base, B . Satellite radar can, however, be used for good stereo if two different look angles Ω' , Ω'' are realized in the two orbits.

4.7 Numerical stereo results with actual radar images

Table V is a compilation of radar stereo results obtained by various authors in the past. A definite quantitative conclusion on stereo accuracy is not possible at this time, the variation of the results is caused by the fact that various systems were used: with/without antenna stabilization; with low/high flying aircraft; in/outside atmospheric turbulences; and with low/high density of ground control etc. A conclusion can only be drawn to the effect that a great variation in achieved accuracies has been reported, ranging from the ground resolution up to many times the resolution. Controlled experiments would be required to obtain a more

TABLE V
Radar stereo accuracies obtained by various authors

Source	Year	Accuracy (meters)			Control per 100 km ²	Resolution (ground-meters)	Antenna		Radar system code	Remarks
		Along 1 σ	Across 1 σ	Height 1 σ			Stabilized	Type		
Gracie	1970	12.2	7.7	13.2	35.0	17	Yes	Synth.	AN-APQ 102	Opp-side
Konecny	1972	68.0	138.0	240.0		17	Yes	Real	Westinghouse	Opp-side
		130.0	428.0	1548.0						Same-side
DBA-Systems	1974	26.8	21.9	16.7	1.2	3	Yes	Synth.	AN-ASQ 142	Opp-side
		29.5	25.6	19.7	3.3	12	Yes	Synth.	GEMS 1000	Same-side
Goodyear	1974			93.0		12	Yes	Synth.	GEMS 1000	Same-side
Derenyi	1975			33.0		12	Yes	Synth.	GEMS 1000	Opp-side
				177.0						Same-side
Leberl	1975	173.0	510.0	109.0	0.3	30-150	No	Synth.	Apollo 17	Same-side, small base, satellite

TABLE VI

Accuracy comparison for various stereo models, using simple parallax measurement techniques

Area	Type of radar	Figure number	Type of measurement	Number of points used	Height error (m)	Correction polynomial
Granite Mountain	Goodyear GEMS	30	Parallax bar	21	78 49	11 Coeff. 17 Coeff.
Granite Mountain	Goodyear GEMS	30	Stereoplotter	21	106 48	11 Coeff. 17 Coeff.
Granite Mountain	SEASAT-SAR optical	33	Parallax bar	28	96 121	17 Coeff. 11 Coeff.
			Stereoplotter	28	121 130	17 Coeff. 11 Coeff.
Los Angeles	SEASAT-SAR optical		Parallax bar	28	143 199	17 Coeff. 11 Coeff.
Los Angeles	SEASAT-SAR digital	34	Parallax bar	28	121 236	17 Coeff. 11 Coeff.

thorough appreciation of the influence of various parameters with real imagery.

Table VI summarizes results obtained with the images of Section 4.3 and of Table III. Stereo measurements were done with a stereoscope and parallax bar to obtain dp , with a digitizer to record r' , r'' , or Ω' , Ω'' , then with a photogrammetric stereo plotting instrument Planimat-D, which was used as a comparator to measure image coordinates x' , y' , x'' , y'' .

Table V leads to the conclusion that the results of aircraft radar with intersection angles of 6° to 20° produce height errors that are only somewhat better than those from SEASAT-SAR with intersection angles 3° to 5° . The reason for the small differences is the fact that look angles with SEASAT are much smaller than with the aircraft data. This compensates to some extent for the poorer intersection geometry. The values conform to the theory. The SEASAT Los Angeles data are poorer than those from Granite Mountain, because intersection angles are more favourable in the latter case. There seem to be no difference between optical and digital correlations when the simple procedures were used that rely on stereoscope and parallax bar.

4.8 Relative orientation – formation of a radar stereo model

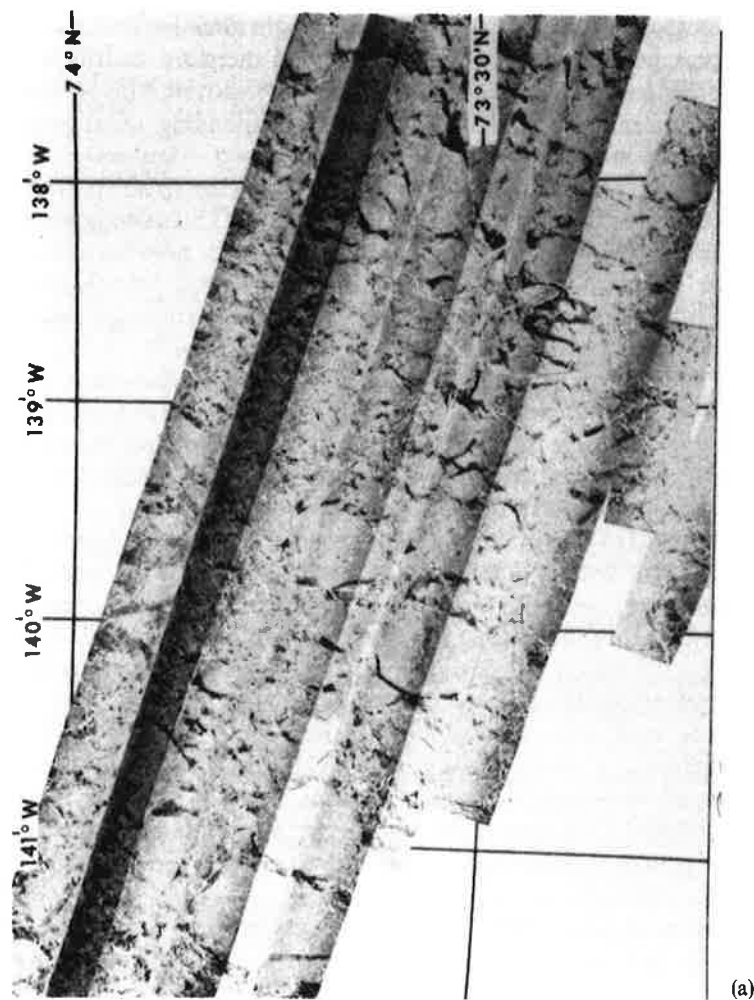
We need a stereo model that has parallaxes in cross-track or y -direction to measure height. Similar parallaxes in flight direction (x -direction) will appear perpendicular to the eyebase and therefore destroy a stereo-impression. These parallaxes must thus be removed. This is equivalent to fulfilment of the conditions that corresponding radar projection circles do intersect one another.

It was assumed in the previous sections that the sensor positions and attitudes for the stereo image pair were known. This assumption cannot be more than an approximation. Errors of sensor position and attitude exist. They must be eliminated to ensure that homologue radar projection circles indeed do intersect, even if there are no ground control points used ("relative orientation of the image pair").

The solution of this problem is of photogrammetric interest. So far no effort has been reported to propose and analyse solutions. Numerically, one can improve the measured or assumed elements of the sensor position and attitude through the formulation of conditions that homologue projection circles must intersect.

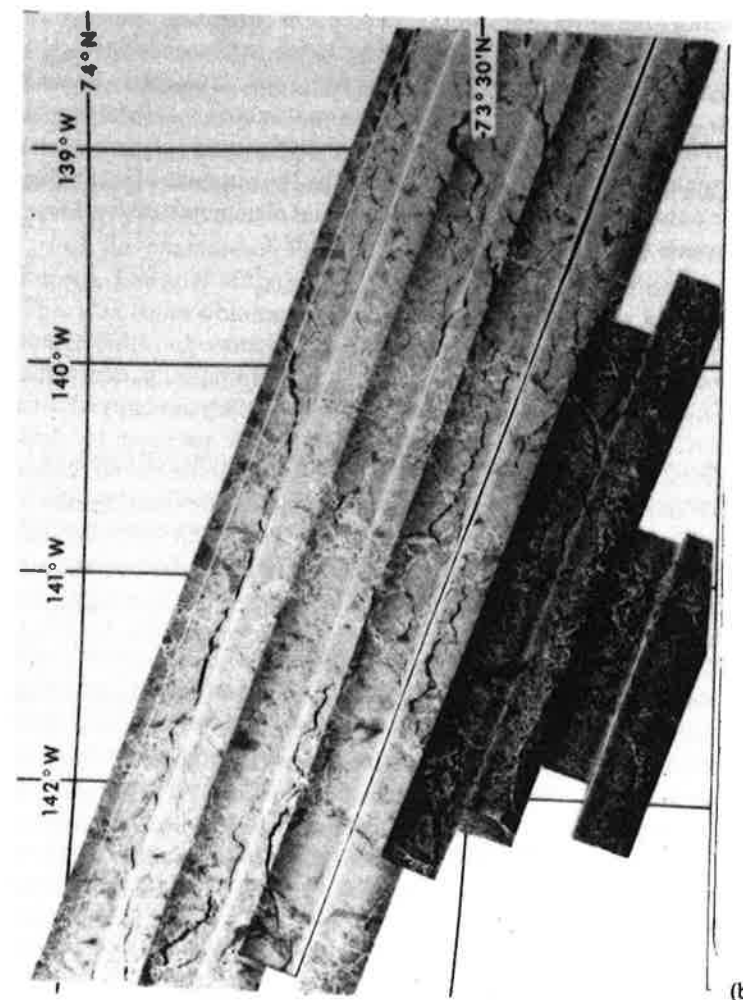
It is easily apparent, that with dynamically acquired imagery only one image line with $x' = \text{constant}$ has one set of position and attitude parameters; along the image, these parameters change as a function of time (compare Section 3.2). But the points of one image line $x' = \text{constant}$ do not all lie on one image line $x'' = \text{constant}$ in the stereo partner. Therefore conditions can only be formulated for individual pairs of points, each time addressing a different set of left and right sensor positions, s' , s'' and attitude \underline{s}' , \underline{s}'' . A single condition only allows one to compute one single parameter, not more. Thus this approach is not very meaningful. One must develop strategies that enable one to ensure the intersection of projection circles, thereby establishing values for the sensor parameters.

Stereo with dynamically acquired images has been studied by Derenyi (1970). His results concern single flight stereo scanning and slit photography. Therefore they are not directly applicable to radar stereo from two flights. On the other hand, the work of Gracie *et al.* (1970), DBA-Systems (1974) and Dowideit (1977) basically proposes numerical solutions with ground control points, without explicit reference to enforcement of intersecting projection circles without the use of control points. Only Norvelle (1972) had to address this question, since he had to



(a)

FIGURE 47 Block of overlapping radar images of arctic sea-ice (a) of 10 October 1975, and (b) of 26 October 1975. Images flown by Jet Propulsion Laboratory (NASA), using an SAR at 25 cm wavelength, 10 km altitude, in the Arctic Ice Dynamics Joint Experiment (AIDJEX).



(b)

create continuous contour lines of imaged terrain. A stereo model was thus required that continuously presented an undisturbed stereo effect to the operator. However, the proposed solution resembles those of the other authors and does not discuss the relative orientation as such.

A successful method has thus so far not been developed. It must, however, operate with a model for sensor exterior orientation as described in Section 3.2; the sensor position and attitude elements must be represented by a limited set of mathematical parameters whose values are to be computed rather than the individual element at each relevant sensor events time.

4.9 Generation of terrain contour lines

Hockeborn (1971) reported on the first radar mapping effort that resulted in (preliminary) contour lines of a previously unmapped area. Norvelle (1972) developed a computer program package to draw contour lines on a computer controlled photogrammetric stereo plotter. Leberl (1976a) presented contour lines of a lunar feature using Apollo 17 stereo radar. Yoritomo (1972) and Graham (1972) both reported on a technique to create digital topographic height data with both stereo and single flight interferometric radar techniques. This technique has subsequently not been pursued. But it was also evaluated by DBA-Systems (1974) without reference to contouring.

The use of radar for height mapping has thus been discussed and demonstrated on several occasions. However, stereo radar was motivated more by its significance for photo-interpretation than for contouring. The acquisition of terrain heights as a final product is expected to be only meaningful in special cases (planetary exploration such as of Venus), or if the sensor position and attitude measurements can be performed with sufficiently high accuracy such that the resulting stereo heights present an accuracy that is meaningful. This would be the case if 20 m contouring were feasible, corresponding to errors of individually measured points of about ± 7 m.

The use of terrain heights from stereo for subsequent generation of an orthophoto is certainly meaningful if the ortho image is needed (compare Section 3.3). The achievable accuracy of heights is expected to be sufficient to correct effects of relief in individual radar images. However, in that case the height data are not a final product but merely serve to create the rectified image as a final result.

5 BLOCKS OF OVERLAPPING RADAR IMAGES

5.1 Definitions and methods

Figure 47 is an illustration of a so-called *block* of overlapping radar imagery. The problem exists to generate ground coordinates of objects radargrammetrically based on: image coordinates of the point in all images that show that point; ground control points; tie points containing overlapping images; and possibly sensor orientation and position parameters.

For the example of Figure 47 several ground control points were known. The goal of the survey was the measurement of sea-ice motion. This was to be obtained from two independent maps based on radar image block adjustment. The difference of point coordinates in the two maps is due to ice motion.

This can be solved by:

- (i) identification and measurement of image tie and control points;
- (ii) transformation of image coordinates of each image strip to the ground system using the equations of Section 3;
- (iii) creation of an image block using tie points;
- (iv) fitting of the block into the pattern of ground control points.

The first step (i) is straightforward. *Tie points* are identical points in adjacent images designed to tie these together. Step (ii) can be applied to individual images producing object p_x, p_y -coordinates if the object is flat, such as in the case with arctic sea ice; or this step can involve a stereo model formation producing p_x, p_y, p_z -coordinates.

The result after step (ii) is erroneous due to errors of sensor position and attitude. A nominally rectilinear flight is in fact along an S-shaped curve. The so-called inertial navigation of aircraft will direct an aircraft nominally along a straight line. A system error will, however, create the flight curvature with a period about 1.5 hours flying time and amplitudes of several kilometers. This error has been explained by Schuler and is named after him (van Roessel and de Godoy, 1974; Leberl, 1975c, 1975d). The type of error is illustrated in Figure 48.

Step (iii) is thus designed to eliminate the Schuler-effect using conditions so that points from adjacent, but overlapping images, should have the same coordinate. Figure 49 illustrates the concept of this so-called "internal block adjustment". For each image a deformation

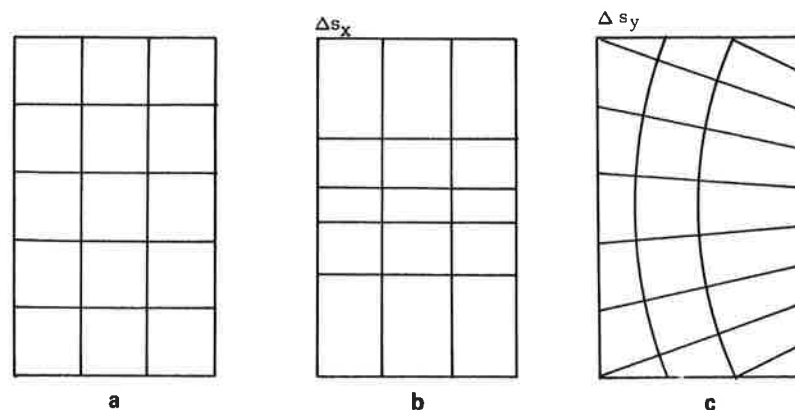


FIGURE 48 Typical errors of synthetic aperture radar image strips: (a) is an underformed grid; (b) an effect of erroneous aircraft speed; and (c) an effect of flight curvature.

$\Delta x(x)$, $\Delta y(x)$ is assumed and modelled with e.g. a spline function.

The result of the internal adjustment is in the form of unique block-coordinates for each point. These need now to be transformed into the object system with ground control points. Any of a number of transformation and interpolation methods is applicable for this purpose (compare Section 3.2.1).

The described method of mapping with a block of images is currently used in operational mapping projects. It was described in detail by Leberl (1975c, 1975d). It corresponds to methods in photogrammetry and photographic image block adjustment. Schut (1970) described it using photogrammetric strips that form a block.

In an experiment, Leberl *et al.* (1976) evaluated several techniques to map areas and demonstrated that this method is superior to those where flights are tracked by Shoran, or where tie-strips are flown to connect production images to a block.

More rigorous and even three-dimensional (x , y and z) methods of radar block mapping were discussed by DBA-Systems (1974) and by Dowideit (1977). The sensor parameters of exterior orientation were described by polynomials or Fourier series (compare Section 3.2.2). However, the demonstrated performance was limited to sets of three small image segments. The robustness of the technique was not discussed.

No further work has been reported on radar blocks, essentially

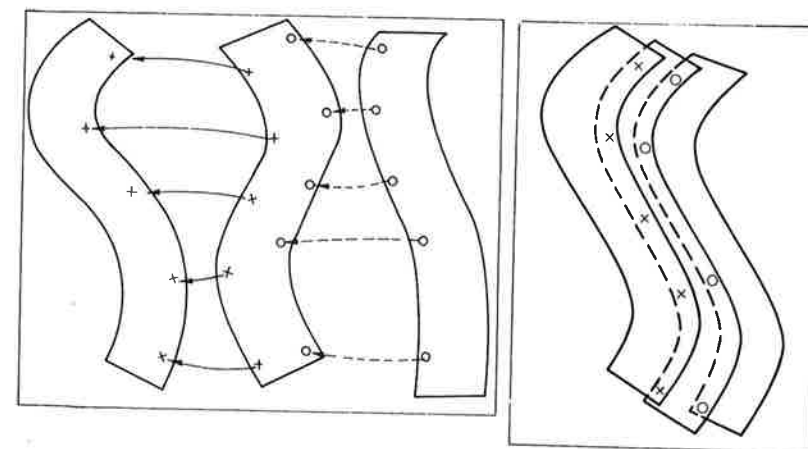


FIGURE 49 Internal adjustment of a radar image block: (a) input; (b) output.

because radar image block mapping is a rare occurrence and therefore does not justify sizeable research and development efforts.

5.2 Results

Numerical results from radar mapping efforts with image blocks exist using simulated data (Leberl, 1975d) as well as from operational projects, e.g. Brazil (van Roessel and de Godoy, 1974), in Colombia (Leberl, 1975c), and in West Virginia (Leberl *et al.*, 1976).

Simulated data permitted comparison of computational techniques leading to the conclusion that spline modelling is distinctly superior to other investigated methods of internal block adjustment. In Brazil's RADAM no block adjustment was performed, but external control of each image flight with Shoran was used. The accuracies amounted to ± 0.5 km for a radargrammetrically computed point.

In Colombia's PRORADAM (Figure 50), images were flown with 63% sidelap (Figure 51).

Tie-point transfer from one image to the next had errors of ± 130 m in the terrain. The radar block deformations amounted to ± 2.2 km prior to correction. After adjustment, and independent comparison with LANDSAT-satellite images demonstrated that radargrammetric coordinates deviated from LANDSAT-coordinates by about ± 400 m. This combines radar and LANDSAT errors.

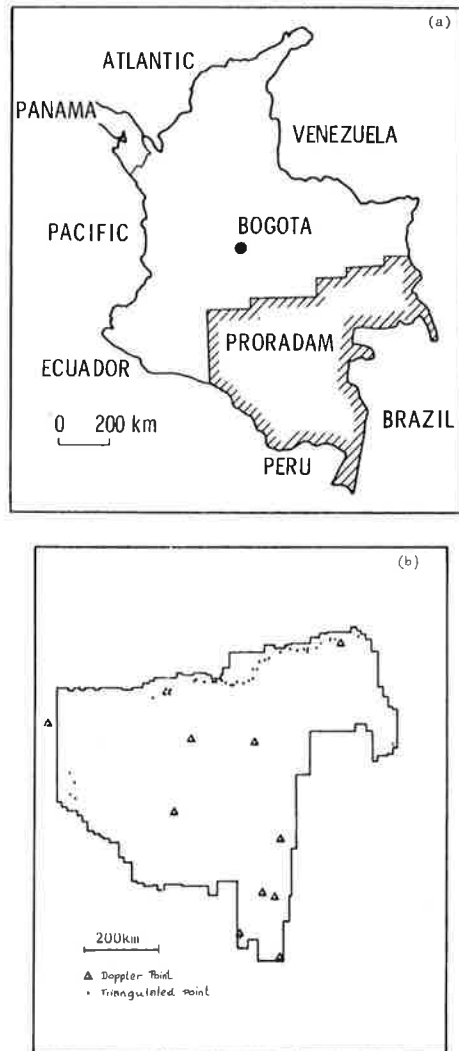


FIGURE 50 (a) Colombia's PRORADAM; (b) control point location.

A more complete numerical evaluation of a radar block was feasible with data from a well-mapped area in the USA (Figure 52). A 20% side-lap was generated of a 90 000 km² area in West Virginia. Tie-point transfer was accurate to within ± 25 m. A graphical presentation of the

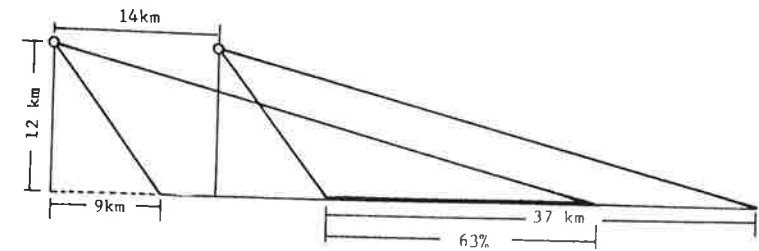


FIGURE 51 Flight configuration for operational radar mapping in Colombia's PRORADAM.

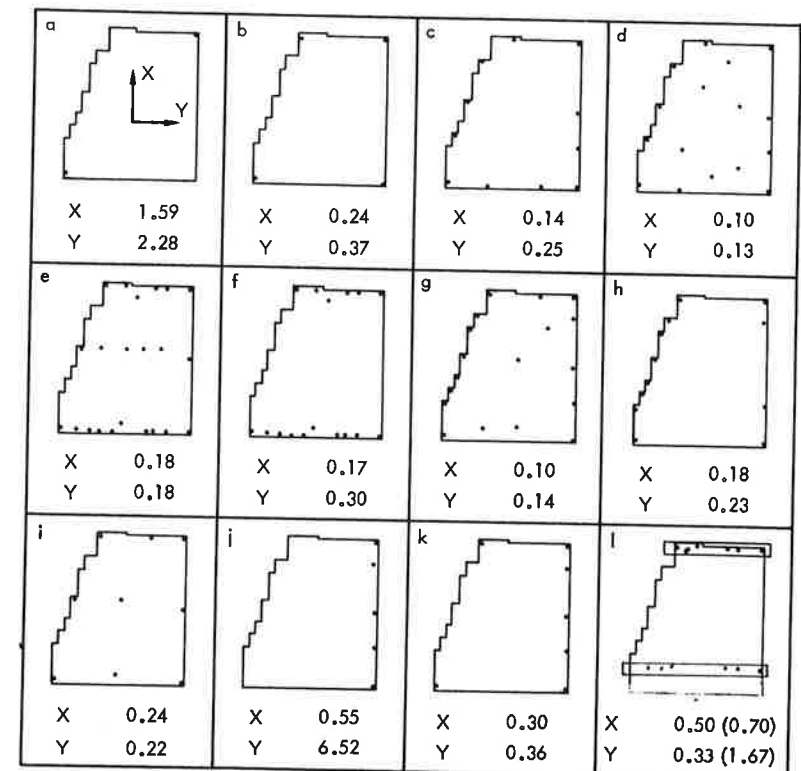


FIGURE 52 Results of block adjustment in West Virginia. Values are in km.

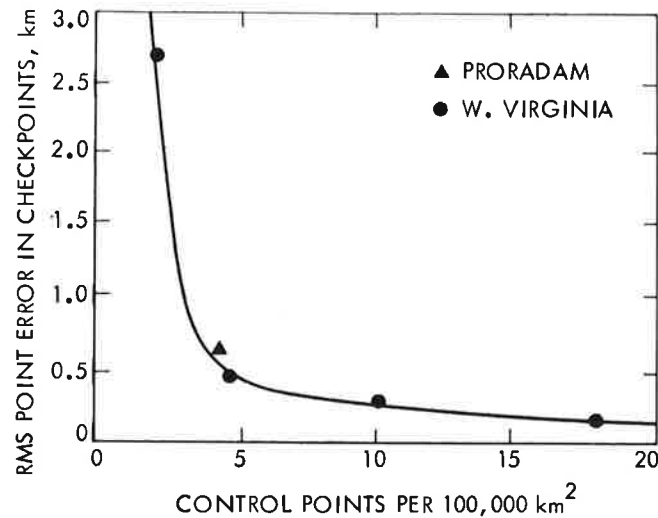


FIGURE 53 Control point density and radar block adjustment result.

radar block adjustment result is shown in Figure 53. It clearly reveals that accuracies approximate ± 100 m, for control of 20 or so points per 100 000 km².

5.3 Discussion

These results demonstrate that radar blocks have led, so far, to modest accuracies. With a ground resolution of, say, 10 to 25 m, a coordinate error of more than ± 100 m is achieved, however with extremely sparse use of ground control points. The purpose of radar imaging of large areas is rapid reconnaissance mapping without dense ground control. Typical scales are 1:200 000. However, the achieved accuracies would remain modest even with denser control unless the following conditions are met:

- (i) imaging is with better internal stability of the sensing device;
- (ii) sensor position and attitude are less affected by short periods, high frequency disturbances, and are measured with higher accuracy;
- (iii) the stereo configurations are optimised for high accuracy.

In particular the future global positioning system (GPS) promises to greatly improve item (ii). GPS-positioning in conjunction with inertial

navigation potentially can get the sensor position measured to within several meters in real time.

Digital radar will eliminate current problems of the internal image geometry (Curlander, 1981). The attachment of sensor events time and slant range to each digital image pixel should be practical to within the geometrical sensor resolution. It is thus to be expected that mapping at scale 1:50 000 will be feasible from future radars.

The third coordinate will remain a problem. Stereo configurations for high vertical accuracy of better than 10 m will be difficult to realize due to viewing limitations. However, the heights will be sufficient to correct image contents for planimetric mapping. This is the more relevant element of mapping efforts due to the continuous changes caused by construction etc., which affect planimetry, but hardly ever height.

6 OUTLOOK

Currently available radar images have geometrical resolutions of about ± 3 to 25 m. They exist from aircraft and, in an experimental context, from spacecraft (Apollo 17, SEASAT and Space Shuttle SIR-A). Operational applications are for small scale 1:200 000 planimetric reconnaissance type mapping of previously unexplored areas, and for surveillance purposes in coastal and arctic environments. The geometric accuracy is not of great concern. It is the interpretation of image details that is the focus.

However, several radargrammetric concepts are of relevance today and may gain weight as and if radar increases in importance for remote sensing from both aircraft and satellites. These concepts are:

- (i) providing a geographic location for each image point;
- (ii) rectifying a given radar image to generate a map-like *ortho-radar-image*;
- (iii) exploring and developing optimum radar stereo capabilities for enhanced image interpretation and the reconstruction of the third dimension of the object;
- (iv) assisting in the systematic and repeated coverage of larger areas with blocks of images and develop concepts to efficiently and rapidly convert them into maps;

(v) participating in the creation of real or near real time monitoring systems of rapidly changing phenomena, such as sea ice, coastal traffic etc.;

(vi) processing of radar together with other data to create image synergisms and image-based information systems.

The work required depends on the further role that radar images are going to play for the observation of the Earth's surface and of other planets. Promises exist of future satellite radar (Space Shuttle SIR-B, Canada's surveillance satellite SURSAT, the European Space Agency's ERS-1, the Japanese ERS-1 and the NASA Venus Radar Mapping mission etc.), and of miniaturized, multi-frequency, all-digital aircraft SAR. If this indeed materializes, then clearly digital radargrammetry needs to be developed with rigorous mathematical models, aiming not merely at a fast and often improvised solution, but at the optimum radargrammetric performance.

The current perspective seems to point to an all-digital radargrammetry instead of today's hybrid techniques, where analog recordings on film are presented to an observer who then takes measurements that are subsequently treated digitally. Radar sensors will be digital camera substitutes or complements, before the digital central perspective camera will be widely available. Therefore digital radargrammetry can obtain a role in the future that may carry more weight in relation to camera photogrammetry than it currently has.

Thus the main advances in radargrammetry must also be the incorporation of digital image processing technology into the image analysis repertoire. The improvement of geometric resolutions, navigation parameter estimation and wide availability are not the responsibility of this field, but do affect it greatly.

An essential tool for radargrammetric method development and evaluation should be image simulation. There are several open areas of significance in radargrammetry that could benefit from the availability of digital image simulation systems. Such open areas are stereo, image rectification and mosaicking, multi-spatial data analysis and creation of image synergisms etc.

Within the field of general purpose mapping of planimetry, radar has played only a modest role so far, totally dominated by aerial photography. The situation is more distinct even regarding height mapping. However, new mapping tasks are emerging that previously did not exist.

They all relate to the concept of monitoring of changing phenomena. It is in this context that mapping by radar has a potential role to play in the future.

Acknowledgements

This paper has been supported in part by research contract 6.931/3-27/1980 of the Austrian Ministry of Science and Research under the direction of Dipl. Ing. Zellhofer. The help of Dipl. Ing. J. Raggam is acknowledged who performed some of the experiments with stereo and with SEASAT radar.

References and Bibliography

- Akowetzky, W. I. (1968). On the transformation of radar coordinates into the geodetic system, *Geodezia i Aerofotosjomka* (in Russian).
- Ambrose, W. (1967). A radar image correlation viewer, *Photogramm. Eng.*, **XXXIII**.
- Azevedo, L. de (1971). Radar in the Amazon, *Proc. 7th Int. Symp. Remote Sensing of the Environment*, Ann Arbor, Michigan.
- Bair, G. L. and G. E. Carlson (1974). Performance comparison of techniques for obtaining stereo radar images, *IEEE Trans. on Geoscience Electronics*, **GE-11**.
- Bair, G. L. and G. E. Carlson (1975). Height measurement with stereo radar, *Photogramm. Eng. and Remote Sensing*, **XLI**.
- Berlin, L. G. and G. E. Carlson (1974). Radar mosaics, *The Professional Geographer*, **XXIII**(1).
- Bicknell, T. et al. (1975). A study to determine the feasibility of using radar techniques for public land surveying, Jet Propulsion Laboratory Report under contract to the Bureau of Land Management, Contract No. 5300-PH-995, Pasadena, California.
- Bosman, E. et al. (1971). Project Karaka—the transformation of points from side looking radar images into the map system, Final Report, Part 1, Netherlands Interdepartmental Working Community for the Application and Research of Remote Sensing Techniques (NIWARS), Delft.
- Bosman, E. R., E. Clerici, D. Eckhart and K. Kubik (undated). Project BEBLOKA—the transformation of points from overlapping images obtained with different sensors into the map system, Final Report, Netherlands Interdepartmental Working Community for the Application and Research of Remote Sensing Techniques (NIRWARS), Delft.
- Bosman, E. R., E. Clerici, D. Eckhart and K. Kubik (1972). KARIN—a program system for the mapping of remote sensing information, pres. paper, *12th Congress, Int. Soc. Photogrammetry*, Ottawa, Canada; and Final Report, Netherlands Interdepartmental Working Community for the Application and Research of Remote Sensing Techniques (NIRWARS), Delft.
- Brown, E. et al. (1981). Application of Seasat SAR digitally correlated imagery for sea ice dynamics, invited paper, *1981 AGU Meeting*, Baltimore, USA.
- Bryan, M. L., W. Stromberg and T. Farr (1977). Computer processing of SAR L-band imagery, *Photo. Eng. and Remote Sensing*, **43**(10), pp. 1283–1294.
- Carlson, G. E. (1973). An improved single flight technique for radar stereo, *IEEE Trans. on Geoscience Electronics*, **GE-11**, No. 4.
- Claveloux, B. A. (1960). Sketching projector for side looking radar photography, *Photogramm. Eng.*, **XXVI**.

- Crandall, C. J. (1963). Advanced radar map compilation equipment, *Photogramm. Eng.*, XXIX.
- Crandall, C. J. (1969). Radar mapping in Panama, *Photogramm. Eng.*, XXXV.
- Curlander, J. (1981). Geometric and radiometric distortion in spaceborne SAR imagery, invited paper, NASA Workshop on Registration—Rectification for Terrestrial Applications, November 17–19, Jet Propulsion Laboratory, Pasadena, USA.
- Curlander, J. (1981). Sensor to target range determination, JPL-Interoffice Memorandum 334.7-80-056, Jet Propulsion Laboratory, Pasadena, USA.
- Daily, M. et al. (1978). Application of multispectral radar and Landsat imagery of geologic mapping in Death Valley, JPL-Publication, 78-19, pp. 47, Pasadena, USA.
- Dalke, G. et al. (1968). Regional slopes with non stereo radar, *Photogramm. Eng.*, XXIV.
- DBA-Systems (1974). Research studies and investigations for radar control extensions, Defense Documentation Center Report No. 530784L, DBA-Systems, Inc., P.O. Drawer 550, Melbourne, Florida.
- Dellwig, I. F. (1980). A new look at Togo through the eyes of a SLAR, in *Radar Geology, an Assessment*, JPL-Publication 80-61, Jet Propulsion Laboratory, Pasadena, USA.
- Derenyi, E. E. (1970). *An Exploratory Investigation into the Relative Orientation of Continuous Strip Imagery*, Ph.D. Thesis and Research Report No. 8, Univ. of New Brunswick, Canada.
- Derenyi, E. E. (1972). Geometric consideration in remote sensing, *Proc. 1st Canadian Symp. on Remote Sensing*, Ottawa.
- Derenyi, E. E. (1974a). SLAR geometric test, *Photogramm. Eng.*, XL.
- Derenyi, E. E. (1974b). Metric evaluation of radar and infrared imageries, *Proc. 2nd Canadian Symp. on Remote Sensing*, Univ. of Guelph, Guelph, Ontario.
- Derenyi, E. E. (1975a). Topographic accuracy of side looking radar imagery, *Bildmessung und Luftbildwesen*, 1.
- Derenyi, E. E. (1975b). Terrain heights from SLAR imagery, pres. paper, 41st Annual Conv. Am. Soc. Photogramm., Washington, D.C., March.
- Dicarlo, C. et al. (1968). All weather mapping, pres. paper, *Int. Congress of Surveyors (FIG)*, London.
- Dicarlo, C. et al. (1971). DoD data processing equipment for radar imagery, pres. paper, *Int. Congress of Surveyors*, Wiesbaden.
- Dowideit, G. (1975). A simulation system for theoretical analysis of radar restitution and a test by adjustment, *Proc. Symp. Comm. III, Int. Soc. Photogramm.*, Stuttgart, W. Germany, in *Deutsche Geodaetische Kommission, Reihe B, Heft No. 214*.
- Dowideit, G. (1977a). Eine Blockausgleichung für Abbildungen des seitwärtschauender Radar (SLAR), *Wissensch. Arbeiten der Lehrstühle für Geodäsie etc.*, Nr. 75, Technische Universität Hannover, FRG, pp. 185.
- Dowideit, G. (1977b). Eine Blockausgleichung für Aufzeichnungen des Seitwärts-Radar (SLAR), *Bildmessung und Luftbildwesen*, 45(1), pp. 17–23.
- Egbert, E. (1969). Calculation of ground street lengths and area from radar measurements, Simonnett, D. S. (ed.), *The utility of radar and other remote sensors in thematic land use mapping from spacecraft*, Annual Report, U.S. Geolog. Survey Interagency Report-NASA 140.
- ESA (1981). Announcement of opportunity for participation in the proposed ERS-1 mission, APP (81) 1, Part B.
- Esten, R. D. (1953). Radar relief displacement and radar parallax, USAERDL-Report No. 1294, Ft. Belvoir, Virginia.
- Fiore, C. (1967). Side looking radar restitution, *Photogramm. Eng.*, XXXIII.
- Froidevaux, C. M. (1980). Radar, an optimum remote sensing tool for detailed plate tectonic analysis and its application to hydrocarbon exploration (an example in Irian Jaya, Indonesia), in *Radar Geology, an Assessment*, JPL-Publication 80-61, Jet

- Propulsion Laboratory, Pasadena, USA.
- Geier, F. (1971). Beiträge zur Geometrie des Radarbildes, Diss., Techn. Univ., Graz, Austria.
- Geier, F. (1972). Fundamentals of orientation for radar PPI images with approximated horizontal distances, pres. paper, 12th Congress, Int. Soc. Photogramm., Ottawa, Canada.
- Glushkov, W. M. et al. (1972). Toros-side looking radar system and its application for sea ice condition study and for geologic explorations, pres. paper, 12th Congress, Int. Soc. Photogramm., Ottawa, Canada.
- Goodyear (1972). Flight test report all-weather topographic mapping system AN/ASQ-142, Contract No. F 33657-70-0769, Goodyear Aerospace Corp., Litchfield Park, Arizona.
- Goodyear (1974). Preliminary imagery data analysis Goodyear Electronic Mapping System (GEMS), Goodyear Aerospace Corp., Report GIB-9342, Code 99696.
- Gracie, G. et al. (1970). Stereo radar analysis, U.S. Engineer Topographic Laboratory, Ft. Belvoir, Virginia, Report No. FTR-1339-1.
- Gracie, G. and E. D. Sewell (1972). The metric quality of stereo radar, *Proc. of the Tech. Program, Electro-Optical Systems Design Conference*, New York, 12–14 Sept.
- Graham, L. C. (1970). Cartographic applications of synthetic aperture radar, *Proc. Am. Soc. Photogramm.*, 37th Annual Meeting; and Goodyear Aerospace Corp., Report GERA-1626.
- Graham, L. (1972). An improved orthographic radar restitutor, pres. paper, 12th Congress, Int. Soc. Photogramm., Ottawa, Canada, and Goodyear Aerospace Corp., Report GERA-1831.
- Graham, L. and H. O. Rydstrom (1974). Synthetic aperture radar applications to earth resources development, Goodyear Aerospace Corp., Report GERA-2010, Code 99696.
- Graham, L. C. (1975a). Geometric problems in side-looking radar imaging, *Proc. Symp. Comm. III, Int. Soc. Photogramm.*, Stuttgart, W. Germany, in *Deutsche Geodaetische Kommission, Reihe B, Heft No. 214*.
- Graham, L. (1975). Flight planning for stereo radar mapping, *Proc. Am. Soc. Photogramm.*, 41st Meeting, Washington, D.C.
- Graham, L. (1976). Earth resources radar stereo considerations, Goodyear Aerospace Corp., Arizona Div., AEEM-550, pp. 13.
- Greve, C. and W. Cooney (1974). The digital rectification of side looking radar, *Proc. Am. Soc. Photogramm.*, Annual Convention, Washington, D.C.
- Hirsch, Th. and J. van Kuilenburg (1976). Preliminary tests of the EMI-SLAR mapping quality, Netherlands Interdepartmental Working-Community for the Application and Research of Remote Sensing (NIRWARS), Internal Report No. 39, Delft.
- Hockeborn, H. A. (1971). Extraction of positional information from side looking radar, *Bildmessung und Luftbildwesen*, 39(1).
- Hoffmann, P. (1958). Photogrammetric applications of radar scope photographs, *Photogramm. Eng.*, XXIV.
- Hohenberg, F. (1950). Zur Geometrie des Funkmessbildes, Austrian Academy of Sciences, *Math.-Naturwissenschaftliche Klasse*, Vienna, 2–3.
- Holtzman, I. C. et al. (1977). Radar image simulation: validation of the point scattering method, Report ETL-0017, 1, USA Engineer Topographic Laboratory, Ft. Belvoir, USA.
- IEEE-Conference (1981). IGARSS 81, *Int. Geoscience and Remote Sensing Symp.*, IEEE Catalog No. 81 CH 1656-8.
- Innes, R. B. (1964). Principles of SLAR measurement of the third coordinate of target position, Report of Project Michigan No. 2900-474-T.
- Ito, N. (1981). SAR digital processing system, pres. paper, ISPRS-SAR Working Group II

- 15, 3-4 Dec., Frascati, Italy.
- Jensen, H. (1972). Mapping with coherent-radiation focused synthetic aperture side-looking radar, in *Operational Remote Sensing: An Interactive Seminar to Evaluate Current Capabilities*, *Am. Soc. Photogramm.*
- Jensen, H. (1975). Deformations of SLAR imagery—results from actual surveys, *Proc. Symp. Comm. III, Int. Soc. Photogramm.*, Stuttgart, W. Germany, in *Deutsche Geodaetische Kommission*, Reihe B, Heft No. 214.
- Kober, C. L. et al. (1950). Determination of target height from radar PPI-photographs, Air Force Techn. Report No. 6500, Wright Air Development Center, Ohio.
- Konecny, G. and E. E. Derenyi (1966). Geometric consideration for mapping from scan imagery, *Proc. 4th Symp. Remote Sensing of the Environment*, Ann Arbor, Michigan.
- Konecny, G. (1970). Metric problems in remote sensing, Publications of the International Institute for Aerial Surveying and Earth Sciences (ITC), Series A, No. 50, Delft.
- Konecny, G. (1971). Orientierungsfragen bei Streifenbildern und Aufnahmen der Infrarot-abtastung, *Bildmessung und Luftbildwesen*, 41(1).
- Konecny, G. (1972a). Geometrical aspects of remote sensing, *Arch. Int. Soc. Photogramm.*, 12th Congress, invited paper, Ottawa, Canada.
- Konecny, G. (1972b). Geometrische Probleme der Fernerkundung, *Bildmessung und Luftbildwesen*, 42(2).
- Konecny, G. (1975). Approach and status of geometric restitution for remote sensing imagery, *Proc. Symp. Comm. III, Int. Soc. Photogramm.*, Stuttgart, W. Germany, in *Deutsche Geodaetische Kommission*, Reihe B, Heft No. 214.
- Koopmans, B. (1974). Should stereo SLAR imagery be preferred to single strip imagery for thematic mapping?, *ITC-Journal* 1974-3, Enschede.
- Koopmans, B. (1974). Drainage analysis on radar images, *ITC-Journal* 1973-2, Enschede, Netherlands.
- Korneev, Iu. N. (1978). Analytical method for photogrammetric processing of a single radar photograph, *Geodezia i Aerofotosjomka*, 2, 115-124.
- Kratky, V. (1979). SEASAT orbit effects on imaging geometry of synthetic aperture radar, 3rd *GDTA Symp.*, Toulouse.
- La Prade, G. L. (1963). An analytical and experimental study of stereo for radar, *Photogramm. Eng.* XXIX.
- La Prade, G. L. (1969). Elevations from radar imagery, *Photogramm. Eng.*, XXXV.
- La Prade, G. L. (1970). Subjective considerations for stereo radar, Goodyear Aerospace Corp., Report GIB-9169, and *Photogramm. Eng.*
- La Prade, G. (1972). Stereoscopia—a more general theory, *Photogramm. Eng.*, 38, pp. 1177-1187.
- La Prade, G. (1973a). Stereoscopia—will facts or dogma prevail?, *Photogramm. Eng.*, 39, pp. 1271-1275.
- La Prade, G. (1973b). A more general theory of stereoscopia, Goodyear Aerospace Corp., Arizona Div., GIB-9268, Rev. A, pp. 58.
- La Prade, G. (1975). Addendum to GIB-9169, Subjective considerations for stereo radar, Goodyear Aerospace Corp., Arizona Division.
- La Prade, G. (1975). Stereoscopia, Goodyear Aerospace Corp., Arizona Div., GERA-2120, Code 99696; pp. 57.
- La Prade, G. L. (1975). Radar signature of inverted catenary with equilateral triangular cross section (St. Louis Gateway Arch), Arizona Electronics Eng. Memo. No. 525, Goodyear Aerospace Corp., Arizona Div., Litchfield Park, Arizona.
- La Prade, G. et al. (1980). Stereoscopia, Chap. 10, *Manual of Photogrammetry*, 4th Edition.
- Leberl, F. (1970). Metric properties of imagery produced by side looking airborne radar and infrared line scan systems, Publications of the International Institute for Aerial Survey and Earth Sciences (ITC), Series A, No. 50, Delft.

- Leberl, F. (1971a). Vorschläge zur instrumentellen Entzerrung von Abbildungen mit Seitwärts Radar (SLAR) und Infrarotabstastsystemen, *Bildmessung und Luftbildwesen*, 39.
- Leberl, F. (1971b). Remote sensing.—Neue Methoden zur Wahrnehmung auf Abstand, *Oesterr. Zeitschrift für Vermessungswesen*, No. 6.
- Leberl, F. (1971c). Untersuchungen über die Geometrie und Einzelbildauswertung von Radarschrägaufnahmen, Diss., Techn. Univ., Wien.
- Leberl, F. (1972). On model formation with remote sensing imagery, *Oesterr. Zeitschrift für Vermessungswesen*, 60, pp. 93-61.
- Leberl, F. (1972a). Evaluation of single strips of side looking radar imagery, *Arch. Int. Soc. Photogrammetry*, 12th Congress, invited paper, Ottawa, Canada.
- Leberl, F. (1972b). On model formation with remote sensing imagery, *Oesterr. Zeitschrift für Vermessungswesen und Photogrammetrie*, No. 2.
- Leberl, F. (1972c). Radargrammetria para los intérpretes de imágenes, Centro Interamericano de Fotointerpretación (CIAF), Bogotá, Colombia.
- Leberl, F. (1974). Evaluation of SLAR image quality and geometry for PRORADAM, *ITC-Journal*, 2(4), Enschede.
- Leberl, F. (1975a). The geometry of, and plotting from, single strips of side looking airborne radar imagery, International Institute for Aerial Survey and Earth Sciences (ITC) Technical Report No. 1, Enschede.
- Leberl, F. (1975b). Radargrammetry for image interpreters, ITC Technical Report No. 2, Enschede.
- Leberl, F. (1975c). Radargrammetric point determination PRORADAM, *Bildmessung und Luftbildwesen*, 45(1).
- Leberl, F. (1975d). Sequential and simultaneous SLAR block adjustment, *Photogrammetria*, 31(1).
- Leberl, F. (1975e). Lunar radargrammetry with ALSE-VHF imagery, *Proc. Am. Soc. Photogramm.*, Fall Tech. Meeting, Phoenix, Arizona.
- Leberl, F., T. Farr, L. Bryan and C. Elachi (1976). Study of arctic sea ice drift from L-band side looking radar imagery, *Proc. Am. Soc. Photogramm.*, 42nd Annual Conv., Washington, D.C.
- Leberl, F. (1976a). Mapping of lunar surface from side looking orbital radar images, *The Moon*, 15(3/4).
- Leberl, F. (1976b). Imaging radar applications to mapping and charting, *Photogrammetria*, 32.
- Leberl, F., J. Jensen and J. Kaplan (1976). Side-looking radar mosaicking experiment, *Photogramm. Eng. and Remote Sensing*, XLII.
- Leberl, F. (1977). Radar mapping applications using single images, stereo pairs, and image blocks: methods and applications, *Revista Brasileira de Cartographia*, No. 20, pp. 16-26.
- Leberl, F. and C. Elachi (1977). Mapping with satellite side-looking radar, *Proc. 2nd GDTA Symp.*, St. Mandé, France, pp. 451-465.
- Leberl, F. (1978a). Satellitenradargrammetrie, *Deutsche Geodaetische Kommission*, Series C, No. 239, Munich, 156 pp.
- Leberl, F. (1978b). Current status and perspectives of active microwave imaging for geoscience application, *ITC-Journal*, 1978-1.
- Leberl, F. and H. Fuchs (1978). Photogrammetric differential rectification of radar images, pres. paper, *Symp. of Comm. III of the Int. Soc. Photogrammetry*, Moscow and Mittl. d. geod. Inst. No. 33, TU-Graz, 8010 Graz, Austria.
- Leberl, F. et al. (1979). Mapping of sea-ice and measurement of its drifts using aircraft synthetic aperture radar images, *J. Geophysical Research*, 84(C4), pp. 1827-1935.
- Leberl, F. (1979). Accuracy aspects of stereo-side-looking radar, JPL-Publication 1979-17,

- Jet Propulsion Laboratory, Pasadena, USA.
- Leberl, F. (1980). Preliminary radargrammetric assessment of SEASAT-SAR images, *Mitteilungen der geodatischen Institute*, No. 33, Tech. Univ., A-8010 Graz, pp. 59–80.
- Leberl, F. and E. Clerici (1980). Current status of metric reduction of active sensor data, *Arch. Int. Soc. of Photogrammetry*, 23/B.3, pp. 435–450.
- Leberl, F. (1981). The Venus orbital imaging radar (VOIR) mission, *Proc. Alpbach Summer School*, 29 July–7 August, ESA SP-164.
- Leberl, F., J. Raggam, C. Elachi and W. Campbell (1981). Measuring sea ice motion from Seasat SAR images, invited paper, 1981 AGU-Meeting, Baltimore, USA. Submitted *Journal of Geophysical Research*.
- Leberl, F., H. Fuchs and J. Ford (1981). A radar image time series, *International Journal of Remote Sensing*, 2(2).
- Leonardo, E. (1959). An application of photogrammetry to radar research, *Photogramm. Eng.*, XXV.
- Leonardo, E. (1963). Comparison of imaging geometry for radar and photographs, *Photogramm. Eng.*, XXXIX.
- Leonardo, E. (1964). Capabilities and limitations of remote sensors, *Photogramm. Eng.*, XXX.
- Levine, D. (1960). *Radargrammetry*, McGraw-Hill Book Company, New York.
- Levine, D. (1963). Principles of stereoscopic instrumentation for PPI-photographs, *Photogramm. Eng.*, XXX.
- Levine, D. (1965). Automatic production of contour maps from radar interferometric data, pres. paper, *Fall Tech. Meeting, Am. Soc. Photogramm.*, Dayton, Ohio.
- Lewis, A. J. and H. C. MacDonald (1970). Interpretive and mosaicking problems of SLAR imagery, *Remote Sensing of Environment*, 1(4).
- Ling, C., L. Rasmussen and W. Campbell (1978). Flight path curvature distortion in side-looking airborne radar imagery, *Photogramm. Eng. and Remote Sensing*, 44(10), pp. 1255–1260.
- Loelkes, G. L. (1965). Radar mapping imagery—its enhancements and extraction for map construction, pres. paper, *Fall Tech. Meeting, Am. Soc. Photogramm.*, Dayton, Ohio.
- Loshchilov, U. S. and U. A. Voyevodin (1972). Determining elements of drift of the ice cover and movement of the ice-edge by the air of the TOROS aircraft lateral scan radar station, *Problemi Ariki, Antartiki*, No. 40, pp. 23–30.
- Luchininov, V. S. (1975). Contactless radar mapping of warm valley glaciers—transformation of radar coordinates, transl. from Russian in *Soviet Physics-Technical Physics*, 20(4), 1976.
- Macchia, R. P. (1957). Radar presentation restitutor, *Photogramm. Eng.*, XXIII.
- Manual of Photogrammetry (1966). Photogrammetric and radargrammetric techniques, II, 3rd Ed.
- Martin-Kaye, P. H. A. et al. (1980). Fracture trace expression and analysis in radar imagery of rain forest terrain (Peru), in *Radar Geology, an Assessment*, JPL-Publications 80-61, Jet Propulsion Laboratory, Pasadena, USA.
- Masry, S. E., E. E. Derenyi and B. G. Crawley (1976). Photomaps from non-conventional imagery, *Photogramm. Eng. and Remote Sensing*, XLII(4).
- McKeon, J. B. (1979). Remote sensing of the resources of Los Andes region, Venezuela, Final Report—I, Environmental Research Institute of Michigan, Report 305 200-7-F, Ann Arbor, Michigan.
- Moore, R. K. (1969). Heights from simultaneous radar and infrared, *Photogramm. Eng.*, XXXV.
- Moreira, H. F. (1973). Project RADAM—remote sensing application to environment analysis of Amazon region, 2nd Annual Remote Sensing of Earth Resources Conf., Univ. of Tennessee Space Inst., Tullahoma, Tennessee.

- Naraghi, M., W. Stromberg and M. Daily (1981). Geometric rectification of radar imagery using a digital elevation model, Manuscript in print, *Photogr. Eng. and Remote Sensing*.
- Norvelle, F. R. (1972). AS-11-A radar program, *Photogramm. Eng.*, XXXVIII.
- Peterson, R. K. (1976). Radar correlator geometric control, Goodyear Aerospace Report GIB 9397, Litchfield Park, Arizona; pres. paper, 13th Cong. Int. Soc. Photogramm., Helsinki, Finland.
- Protherse, W. M. et al. (1950). The geometry of the radarscope, techn. paper, No. 107, Mapping and Charting Laboratory, Ohio State Univ., Ohio.
- Radar Geology (1980). *Radar Geology, an Assessment*, JPL-Publication 80-61, Jet Propulsion Laboratory, Pasadena, USA.
- Raney, K. (1981). Radarsat programme, pres. paper, ISPRS-SAR Processing Working Group II 15, Frascati, Italy, 3–4 Dec.
- Raytheon Co. (1973). Digital rectification of sidelooking radar (DRESLAR), final report, Raytheon Co., Automatic Operation, Prop. for U.S. Army Engineer Topographic Laboratories, Ft. Belvoir, Virginia 22060, Report No. ETL-CR-73-18.
- Rinner, K. (1948). Die Geometrie des Funkbildes, Austrian Academy of Sciences, *Math. Naturwiss. Klasse*, also in *Handbuch der Vermessungskunde*, Jordan-Eggert-Kneissl, VI, Metzlersche Verlagsbuchhandlung, Stuttgart.
- Roessel, J. van and R. de Godoy (1974). SLAR mosaics for project RADAM, *Photogramm. Eng.*, XL.
- Rosenfield, G. B. (1968). Stereo radar techniques, *Photogramm. Eng.*, XXXIV.
- Rydstrom, H. C. (1968). Radargrammetric applications of the right angle solution nomogram, Goodyear Aerospace Corp., Report GIB 9124, Litchfield Park, Arizona.
- Scheps, B. B. (1960). To measure is to know—geometric fidelity and interpretation in radar mapping, *Photogramm. Eng.*, XXVI.
- Schertler, R. J. et al. (1975). Great Lakes all-weather ice information system, *Proc. 10th Symp. Remote Sensing of the Environment*, Ann Arbor, Michigan.
- Schreiter, J. B. (1950). Strip projection for radar charting, techn. paper, No. 130, Mapping and Charting Laboratory, Ohio State Univ., Ohio.
- Shakine, A., T. Le Toan (1978). A study of digitized radar images, *Int. Symp. of Remote Sensing of Environment*, Ann Arbor, USA.
- Smith, H. P. (1948). *Mapping by radar—the procedures and possibilities of a new and revolutionary method of mapping and charting*, U.S. Air Force, Randolph Field, Texas.
- Stilwell, J. E. (1963). Radar network adjustment, *Photogramm. Eng.*, XXI.
- Super, A. D. et al. (1975). Remote sensing applied to the international ice patrol, *Proc. 10th Symp. on Remote Sensing of the Environment*, Ann Arbor, Michigan.
- Tiernan, M. et al. (1976). Lunar cartography with the Apollo 17 radar imagery, *The Moon*, 15(1/2).
- Thomann, G. (1969). Distance computation on radar film, Simonnett, D. G. (ed.), *The Utility of Radar and Other Remote Sensors in Thematic Land Use Mapping from Spacecraft*, Annual Report, NASA-140.
- Thompson, T. W. et al. (1972). Progress report on 25 cm radar observations of the 1971 AIDJEX studies, Arctic Ice Dynamics Joint Experiment (AIDJEX) Bulletin, No. 12, Univ. of Washington, Seattle, Washington.
- Yoritomo, K. (1965). All weather mapping, pres. paper, *Fall Technical Meeting, Soc. Photogramm.*, Dayton, Ohio.
- Yoritomo, K. (1972). Methods and instruments for the restitution of radar pictures, *Arch. Int. Soc. Photogramm.*, 12th Congress, inv. paper, Ottawa, Canada.
- Zhurkin, I. G. and N. Korneyev (1974). Relationship between the coordinate of terrain points and the coordinates of image points in side-looking radar systems with an antenna along the fuselage, *Geodesy, Mapping, Photogrammetry*, 16(3), pp. 140–146.

Additional references

- Baker, J. and E. M. Mikkail (1975). Geometric analysis and restitution of digital multispectral scanner data arrays, LARS Information Note 05 28 75, Purdue Univ., USA.
- Ebner, H. and R. Hoessler (1978). The use of Gauss-Markov processes in digital rectification of remote sensing data, *ISP-Comm. III Symp.*, Moscow, pp. 258-265.
- Graham, L. C. (1974). Synthetic interferometer radar for topographic mapping, *Proc. IEEE*, **62**(6).
- Kraus, K. (1976). Anwendungsmöglichkeiten eines digital gesteuerten Differentialumbildegerätes, *Geowissenschaftliche Mitteilungen*, No. 8, pp. 1-22, Technical Univ., Vienna, Austria.
- Leberl, F. (1975f). Photogrammetric interpolation, *Photogramm. Eng.*, **XLI**.
- Makarovic, B. (1973). Digital mono plotters, *ITC-Journal*, 1973-4, Enschede, The Netherlands.
- Manning, B. N. and D. D. Hann (1967). Some simple equations of satellite motion, Arizona Electronics Eng. Memo. No. 267, Goodyear Aerospace Corp., AAP-26297, Litchfield Park, Arizona.
- Mathews, R. E. (ed.) (1975). Active microwave workshop report, NASA Special Report SP-376, Washington, D.C.
- Moritz, H. (1973). Least squares collocation, *Deutsche Geodaetische Kommission*, Series A, Nr. 75, München, W. Germany.
- Phillips, R. J. et al. (1973). Apollo lunar sounder experiment, Apollo 17 Preliminary Science Report, NASA Special Publ. SP-330, Washington, D.C.
- Rinner, K. and W. Burkhardt (1972). *Photogrammetrie, IIIa* of Handbuch des Vermessungswesens, Jordan-Eggert-Kneissl (ed.), 10 Edition, Metzler-Stuttgart, 2371 pp.
- Schut, G. (1970). External block adjustment of planimetry, *Photogramm. Eng.*, **XXXVI**.
- Teleki, P. and R. Ramseier (1978). The Seasat—a synthetic aperture radar experiment, *Proc. Int. Symp. Comm. VII, Int. Soc. of Photogrammetry*, July 2-8, Univ. of Freiburg, 1, 92-114.

Remote Sensing Reviews, 1983, Vol. 1, pp. 159-178
 0275-7257/83/0101-0159\$12.00/0
 © 1983 Harwood Academic Publishers GmbH
 Printed in Great Britain

SECTION 4

Introduction to the Use of Radar in Remote Sensing

L. KRUL

Delft University of Technology, The Netherlands

1 INTRODUCTION

Although operated differently, remote sensing radar is based on the same principles as the "normal" radar used, for example, as a navigation aid. These basic principles are introduced, and the problems related to the observation of distributed targets are dealt with. Special attention is paid to the means by which the geometric resolution can be improved. Finally, the side-looking radar and the synthetic aperture radar are described in some detail.

As is well known, the word "radar" stands for "radio detection and ranging". To this end the target is illuminated by an electromagnetic wave generated by a transmitter. The detection of the target is made possible by part of the incident wave being scattered back in the direction of the receiver, which is generally located by the transmitter. The distance between the radar and the target is derived from the time difference between the transmitted and the received signals. The measurement of this time interval is facilitated by modulating the transmitter with a pulse signal.

The situation described thus far refers to the so-called isolated target, i.e. one single target in an empty space. In most cases, however, the target will be placed in a background and consequently part of this background will contribute to the received signal as well.

These background echos show a noisy character due to the spread in both the arrival time and the amplitude, and therefore tend to disturb the isolated target measurement. The background signal is called "clutter", and, depending on the actual situation, is specified as "rain", "sea" or "ground clutter".